# Prognostic Health Assessment of an Automotive Proton Exchange Membrane Fuel Cell System

by

**Christopher J. Rukas**

A Thesis Submitted in Partial Fulfillment of the Requirements for the Degree of Master of Science
in Mechanical Engineering

Supervised by

Assistant Professor Dr. Jason Kolodziej
Department of Mechanical Engineering
Kate Gleason College of Engineering
Rochester Institute of Technology
Rochester, New York
August 2013

Approved by:

---

Dr. Jason Kolodziej, Assistant Professor
*Thesis Advisor, Department of Mechanical Engineering*

---

Dr. Margaret Bailey, P.E., Professor
*Committee Member, Department of Mechanical Engineering*

---

Dr. Satish Kandlikar, Professor
*Committee Member, Department of Mechanical Engineering*

---

Dr. Alan Nye, Associate Department Head
*Department Representative, Mechanical Engineering*





ProQuest LLC.
789 East Eisenhower Parkway
P.O. Box 1346
Ann Arbor, MI 48106 - 1346

# Thesis Release Permission Form

Rochester Institute of Technology
Kate Gleason College of Engineering

Title:

Prognostic Health Assessment of an Automotive Proton Exchange Membrane Fuel Cell System

I, Christopher J. Rukas, hereby grant permission to the Wallace Memorial Library to reproduce my thesis in whole or part.

---

Christopher J. Rukas

---

Date

# Dedication

This thesis is dedicated to my loving parents James and Carolyn Rukas. Their love, support, and encouragement have made me who I am today.

# Acknowledgments

Foremost, I would like to thank my pricipal advisor Dr. Jason Kolodziej for his patience, motivation, and knowledge. Without his consistent, vigilant support this adventure would not have been possible.

I would like to acknowledge the academic, technical, and financial support of the Rochester Institute of Technology and its faculty.

I thank my dear friends Daniel Geiyer, Jay Wheaton, and Sadaf Mackertich for supporting me these past few years. Our heavily caffienated nights will forever be in my memories.

# Abstract

**Prognostic Health Assessment of an Automotive Proton Exchange Membrane Fuel Cell System**

**Christopher J. Rukas**

**Supervising Professor: Dr. Jason Kolodziej**

Proton exchange membrane fuel cells are a promising technology for the automotive industry. However, it is necessary to develop effective diagnostic tools to improve system reliability and operational life to be competitive in the automotive market. Early detection and diagnosis of fuel cell faults may lead to increased system reliability and performance. An efficient on-line diagnosis system may prevent irreparable damage due to poor control and system fatigue. Current attempts to monitor fuel cell stack health are limited to specialized tests that require numerous parameters. An increased effort exists to minimize parameter input and maximize diagnostic robustness. Most methods use complex models or black-box methods to determine a singular fault mode. Limited research exists with pre-processing or statistical methods. This research examines the effectiveness of a Naïve Bayes classifier on determining multiple states of health; such as healthy, dry, degraded catalyst, and inert gas build-up. Independent component analysis and principal component analysis are investigated for preprocessing. An automotive style fuel cell model is developed to generate data for these purposes. Since automotive applications have limited computational power, a system that minimizes the number of inputs and computational complexity is preferred.

# Contents

# List of Tables

# List of Figures

# Acronyms

**APU** Auxiliary power unit.

**BOP** Balance of plant.

**BPP** Bi-polar plate.

**CBM** Condition based maintenance.

**CI** Current interrupt.

**EIS** Electrochemical impedance spectroscopy.

**ICA** Independent component analysis.

**MEA** Membrane electrode assembly.

**PCA** Principal component analysis.

**PEM** Polymer electrolyte membrane.

**PEMFC** Proton exchange membrane fuel cell.

**PHM** Prognostic health management.

**RUL** Remaining useful life.

# Nomenclature

$a$ Water activity

$A_T$ Nozzle crossectional area ($m^2$)

$C$ Capacitance of a fuel cell (F)

$C_D$ Discharge coefficient

$C_p$ Specific heat at constant pressure J/(kg K)

$C_v$ Specific heat at constant volume J/(kg K)

$D_\omega$ Water diffusion coefficient ($cm^2/s$)

$e$ Charge of an electron (C)

$E$ Open circuit voltage (V)

$F$ Faraday constant (C/mol)

$f_v$ Volume fraction of water

$G_f$ Gibbs free energy (kJ)

$\bar{g_f}$ Gibbs free energy (kJ/mol)

$h$ Specific enthalpy (J/kg)

$h_c$ Convective heat transfer coefficient ($w/m^2$)

$i$ Cell current density ($A/cm^2$)

$i_0$ Exchange current density ($A/cm^2$)

$J$ Inertia (kg m$^2$)

$M$ Molar mass (g/mol)

$m$ Mass (kg)

$Ma$ Mach number

$\dot{m}$ Mass flow rate (kg/s)

$N_A$ Avagadro's number (1/mol)

$N_{fc}$ Number of fuel cells

$p$ Pressure (bar)

$q$ Heat transfer (w)

$\bar{R}$ Universal gas constant (J/(kg K))

$R_{ohm}$ Membrane resistance ($\Omega$)

$T$ Temperature (K)

$t_m$ Membrane thickness (cm)

$U_{cp}$ Compressor blade tip speed (m/s)

$V$ Volume (m$^3$)

$v$ Voltage (V)

$x$ Mass fraction

$y$ Mole fraction

$\mathbf{Z}$ Feature vector

**Greek letters**

$\gamma$ Ratio of specific heats

$\eta$ Efficiency

$\lambda_m$ Membrane water content (mol$_{H_2O}$/mol$_{SOH_3}$)

$\omega$ Humidity ratio

$\phi$ Relative humiditity

$\Phi$ Normalized compressor flow rate

$\sigma_m$ Membrane resistivity (cm/$\Omega$)

$\tau$ Torque ($N - m$)

**Subscripts**

$act$ Activation

$air$ Ambient air

$amb$ Ambient

$a$ Anode

$atm$ Atmosphere

$c$ Cathode

$cl$ Cooler

$clt$ Coolant

$cm$ Compressor motor

$conc$ Concentration

$crit$ Critical

$diff$ Diffused

$dyn$ Dynamic

$fc$ Fuel cell

$H_2$ Hydrogen

$hex$ Heat exchanger

$ha$ Heat exchanger air

$hm$ Humidifier

$inj$ Injected

$i$ Inlet

$l$ Liquid water

$max$ Maximum

$membr$ Membrane

$N_2$ Nitrogen

$O_2$ Oxygen

$ohm$ Ohmic

$o$ Outlet

$rm$ Return manifold

$rx$ Reacted

$sat$ Saturation

$sm$ Supply manifold

$st$ Fuel cell stack

$v$ Water vapor

$w$ Water

# Chapter 1

# Introduction

The Proton exchange membrane fuel cell (PEMFC) is an electrochemical device that converts chemical energy from a gaseous fuel to generate electricity and heat. The fuel cell is an alternative form of energy production for stationary and transportation applications. In this case, hydrogen ($H_2$) is the fuel and oxygen ($O_2$), supplied by ambient air, is the oxidant in the reduction reaction. The PEMFC was first developed for NASA's early manned space vehicles by General Electric in the 1960s [1]. It has great potential in the transportation industry today and is considered more developed for ground vehicle applications than other fuel cell types [2].

Fuel cells are actively studied for use in the automotive industry, for auxiliary power units (APUs) in heavy duty trucks and RVs, for propelling automobiles, generating electricity for individual homeowners, and commercial energy production [1]. In this research, a PEMFC is the focus for propulsion of automotive vehicles. PEM fuel cells are commonly used for automotive applications as high efficiency at partial load makes them likely candidates for urban and highway driving scenarios.

The fuel cell market may decrease our dependencies on fossil fuels with the development of a hydrogen infrastructure and an energy market based off of renewable sources such as wind, hydroelectric, geothermal, or solar power [3, 4]. This has huge implications for national security and sustainable energy practices by removing dependencies on foreign oil.

PEMFC technology is relatively new and limited research exists in PEMFC fault detection. This study will describe the components of a PEM fuel cell stack and the typical

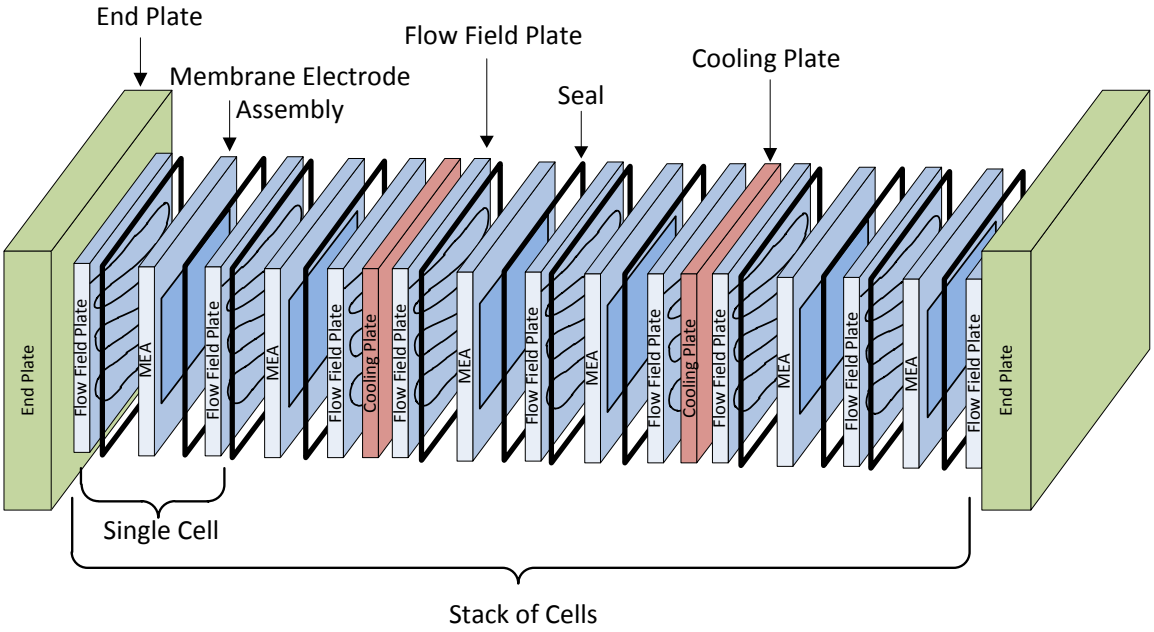


Figure 1.1: Fuel Cell Stack Assembly

equipment required to operate it in an automotive setting. Later, a control orientated automotive fuel cell model is enhanced for use in fault detection and state of health research.

## 1.1 Proton Exchange Membrane Fuel Cell Stack

The proton exchange membrane fuel cell stack is an assembly of PEM fuel cells grouped together in series and attached by bipolar plates which increases the available voltage. A series assembly also allows for compression of the components thus increasing power density. As shown in Figure 1.1, two end plates compress the membrane electrode assemblies, bipolar plates, and cooling plates placed between small assembly groups. A seal is placed between the membrane electrode assembly and the flow field plates thus concluding the fuel cell stack assembly.

### 1.1.1 Membrane Electrode Assembly

The membrane electrode assembly (MEA) is the composition of the anode, membrane, and cathode with their appropriate catalysts. The overall reaction in Equation (1.1) occurs across the MEA. The configuration is shown in Figure 1.2, along with the reaction. Hydrogen ions move across the membrane electrode assembly and bond with oxygen ions to

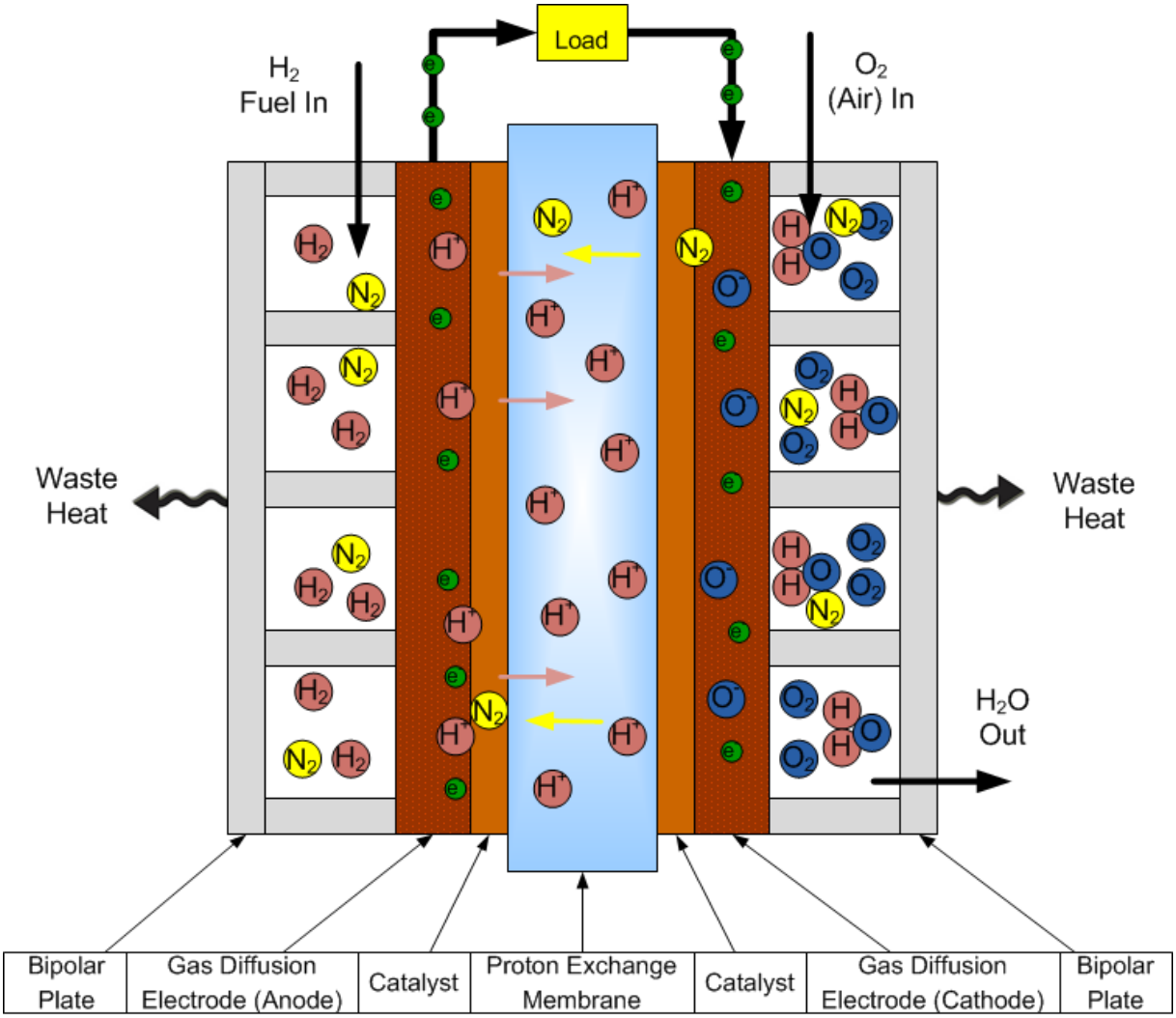


Figure 1.2: Fuel Cell Diagram

generate water, electricity, and heat.

$$2H_2 + O_2 \rightarrow 2H_2O \tag{1.1}$$

**Polymer Electrolyte Membrane**

The polymer electrolyte membrane (PEM) is used to move $H^+$ ions. Sulphonated flouropolymers, usually flouroethylene, are often used as the membrane. One of the most common membranes is Nafion, a product of DuPont, it is considered an industry standard [1].

In constructing a membrane, polyethylene undergoes perflourination and the hydrogen is replaced by flourine generating tetraflouroethylene, also known as Teflon. The material is highly hydrophobic, which helps prevent flooding during operation. The tetrafluoroethylene undergoes sulfonation (addition of a $HSO_3$) to create pockets that are extremely hydrophyllic. Since the $HSO_3$ is bonded ionically, the end of the chain becomes $SO_3^-$. This means the membrane is a mixture of hydrophobic and hydrophyllic regions.

The hydrophyllic regions of the membrane are separated by hydrophobic regions. As the hydrophyllic regions retain water, the distance between them decreases and $H^+$ ions can move more easily. This improves fuel cell performance. Respectively, if the water content decreases the resistance of the membrane will increase, decreasing the fuel cell performance.

**Electrodes**

An electrode is a component that passes current between a metallic part and a non-metallic part in an electrical circuit. An electrode can be an anode or a cathode. Oxidation occurs at the anode, which is the loss of an electron. Reduction occurs at the cathode, which is the gain of an electron. Electrons move from the anode to the cathode, but conventional positive current flows from the cathode to the anode.

The surface area of an electrode in an electrochemical cell is important. The surface area in a PEM electrode cannot be determined by a simple length times width calculation. Roughness is increased so that the real surface area is many times greater than the length times width. Increasing the real surface area increases catalyst utilization by generating

more activity sites.

The anode side is exposed to the fuel hydrogen. The surface of the electrolyte and the electrode ionizes hydrogen and creates the reaction in Equation 1.2.

$$2\,H_2 \rightarrow 4\,H^+ + 4\,e^- \tag{1.2}$$

The cathode side of the MEA is exposed to ambient air (for access to $O_2$). As hydrogen protons move through the membrane towards the cathode water is formed by the reaction in Equation 1.3.

$$O_2 + 4\,H^+ + 4\,e^- \rightarrow 2\,H_2O \tag{1.3}$$

#### Catalyst

A catalyst is added to the PEM to improve the rate of the electrochemical reaction. PEMFCs suffer from inadequate performance on the cathode [5]. Platinum is the most effective catalyst for the electrodes in a PEMFC [1]. Currently, platinum-alloy catalysts are the most practical due to their durability and effectiveness, but non-precious metal catalysts are studied too [5, 6]. Early PEMFC designs required 28 $mg/cm^2$ of Platinum, but this has since been significantly reduced to an approximate 0.2 $mg/cm^2$ [1].

### 1.1.2 Additional Hardware

#### Bi-Polar Plate

The bi-polar plate (BPP) is an interconnecting device with multiple functions. It provides channels for hydrogen and air on either side, and sometimes contains coolant channels. A variety of flow patterns exist for the reactants. There are a variety of materials and methods used to create the BPP which accounts for 30% of the cost and 80% of the weight in the fuel cell stack.

Several flow pattern designs are presented in Figure 1.3. Each flow pattern has its own advantages and disadvantages. Water droplets are not pushed out effectively in parallel designs (see Figure 1.3b). The serpentine design has more saturation and higher temperatures at the exit than other designs (see Figure 1.3a). The mixed design (Figure 1.3c) attempts

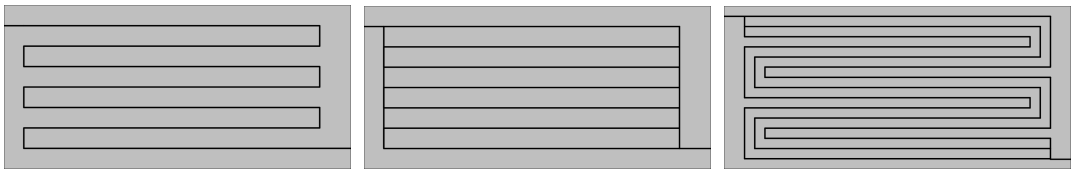

(a) Serpentine (b) Parallel (c) Mixed

Figure 1.3: Flow Path Patterns

to minimize these problems. The channel cross sections are typically square, even though other designs have been explored. A more in-depth review is found in [7].

#### Cooling Plate

The cooling plate (when used) is interspersed between groups of fuel cells as shown in Figure 1.1 [7] . The cooling plate is used to remove heat generated from the fuel cell stack. The spacing is optimized to reduce thermal stresses without introducing excess material. In some situations, the cooling plate is integrated into the BPP.

Deionized water or a similar low conductivity fluid flows through the cooling plate. A coolant with low conductivity minimizes electrical losses in the system.

#### End Plate

The end plate is similiar to the bipolar plate, except that it will only disperse a reactant on one side [7, 8]. It is important that the end plates generate uniform compression on the fuel cell stack. Non-uniform pressure distributions caused by non-uniform compression will cause a non-uniform current distribution [8]. Non-uniform currents lead to hot spots which may destroy the MEA.

## 1.2 Balance of Plant

The balance of plant (BOP) of a fuel cell stack varies depending on operating pressures, temperatures, and energy production. Many configurations exist but most are comprised of the following elements. Pumps exist for recirculating hydrogen, moving coolant, and moving air. Air can be compressed or blown. A humidification system can be included

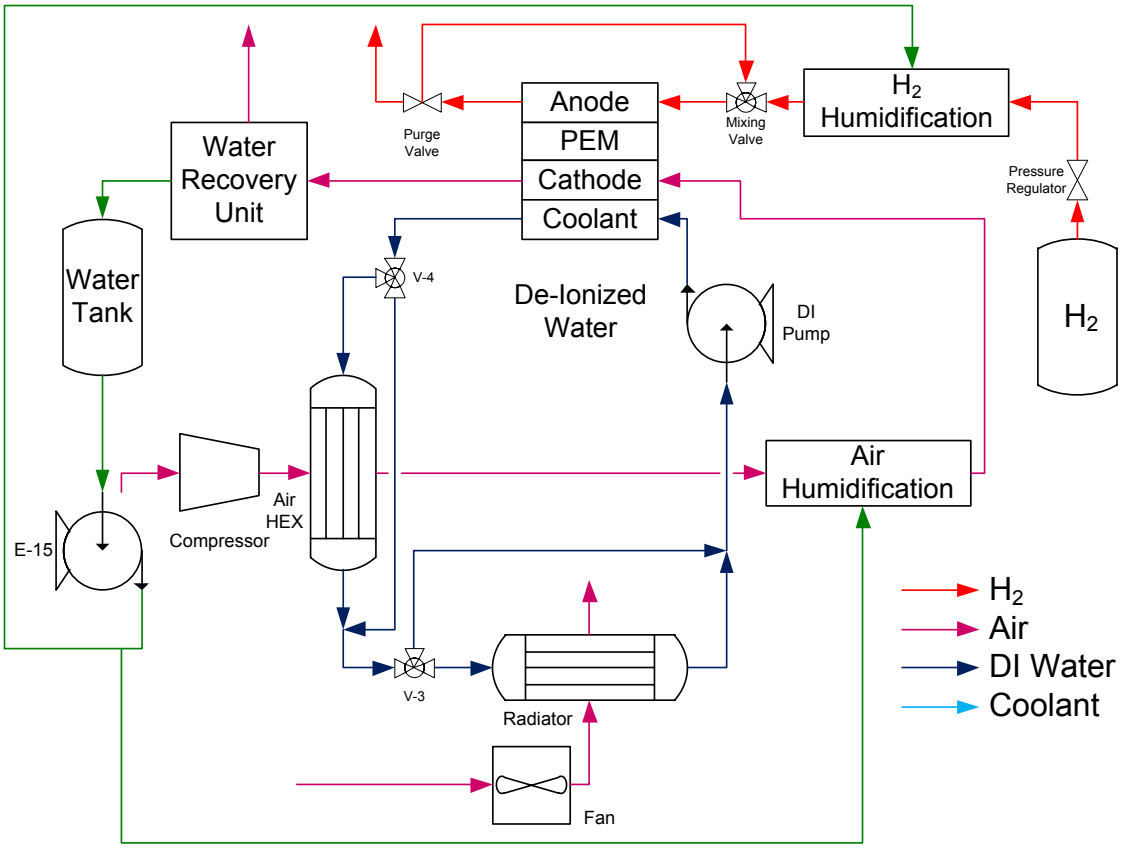


Figure 1.4: Balance of Plant Configuration

to humidify the inlet air and inlet hydrogen. An on-board computer (electronic controller) is used to manipulate the various pumps and valves involved. An example configuration is shown in Figure 1.4 where two coolant loops exist to maintain stack temperature and reduce compressed air temperature. A hydrogen humidification system is incorporated to improve anode humidity, and a similiar system exists for the cathode. The cathode also includes a water recovery unit to humidify cathode inlet air.

**Gas Management**

Gas can be moved through a variety of methods. These include pumps, compressors, ejectors, and fans. Compressors offer large changes in pressure. Fans move significantly less air and have very little change in pressure. Ejectors are a method of circulating hydrogen

by releasing a high pressure source into a low pressure volume.

Hydrogen is compressed into high pressure cylinders unless some method of fuel reformation is involved. A pressure regulating valve is used to maintain operating pressure at the anode. Since the hydrogen fuel is compressed, ejectors can be used instead of fans or pumps to encourage hydrogen circulation.

A blower or compressor is used to increase the air flow rate and pressure across the fuel cell. Increased air flow decreases activation losses. A compressor is used to improve the fuel cell reaction rate, improving fuel cell efficiency [9].

**Water Management**

Water management is the control of liquid and vapor water within the fuel cell stack. Humidifying the gases prevents dehydration of the MEA but overhumidification causes reactant starvation due to liquid water accumulation in the reactant flow channels [10]. Ion conductivity is improved with a well hydrated MEA, improving fuel cell efficiency [1, 10, 11]. De-ionized water is required for the humidifier to minimize contamination of the fuel cell [9].

Two types of gas humidification exist, external and internal humidification. Membrane humidifiers, steam injectors, bubblers, enthalpy wheels, and sprayers are all external humidifiers. These methods have high parasitic losses and increase system complexity and cost [10]. Internal humidification can be accomplished by re-using the reactant gas. Air that exits the fuel cell is at a higher temperature and higher humidity. This air can be mixed with the inlet air to increase the humidity [10]. Internal humidification does not work well during start-up when the MEA is dry [11]. However, diffusive humidifiers are cheap in comparison to external humidification techniques [11].

**Thermal Management**

The temperature is controlled either by coolant or cathode air flow. Larger stacks that generate more heat require some sort of coolant system. Small stacks can be cooled by adjusting the cathode air flow rate. Just like the humidification system, the coolant is required

to be de-ionized [9].

If coolant is used to maintain stack temperature, the system will have a radiator, a fan, a pump, a bypass loop, and a heat exchanger for the compressor output. The bypass loop is used to keep coolant flowing through the fuel cell stack (to encourage a uniform temperature distribution) while neglecting the heat exchanger. The coolant flow rate through the heat exchanger is controlled to increase or decrease coolant temperature, thus controlling stack temperature.

#### Controller & Electrical Equipment

Fuel cells have a variety of electrical components ranging from sensors, heaters, and controllers. Hybrid systems of fuel cells and batteries/capacitors are used to improve transient responses [12].

## 1.3 Voltage Characteristics

Proton exchange membrane fuel cell voltages are defined by their voltage losses. These losses can be temporary and recoverable or permanent. A recoverable voltage loss represents a temporary loss in efficiency due to removable contaminants, humidity issues, or control related issues. A permanent voltage loss may occur from contamination or physical degradation due to aging or poor control. This research seeks to differentiate the three main voltage loss regions. These are activation, ohmic, and mass transport (concentration, fuel starvation) losses. Figure 1.5 shows each loss and how it affects the polarization curve. The activation losses take effect at low current densities. Ohmic losses linearly increase with current and dominate the center of a polarization curve, while mass transport losses take effect at high current densities. These each degrade from the open circuit voltage.

The equation to model the polarization curve follows

$$V = E_0 - \Delta V_{Activation} - \Delta V_{Ohmic} - \Delta V_{MassTransport} \tag{1.4}$$

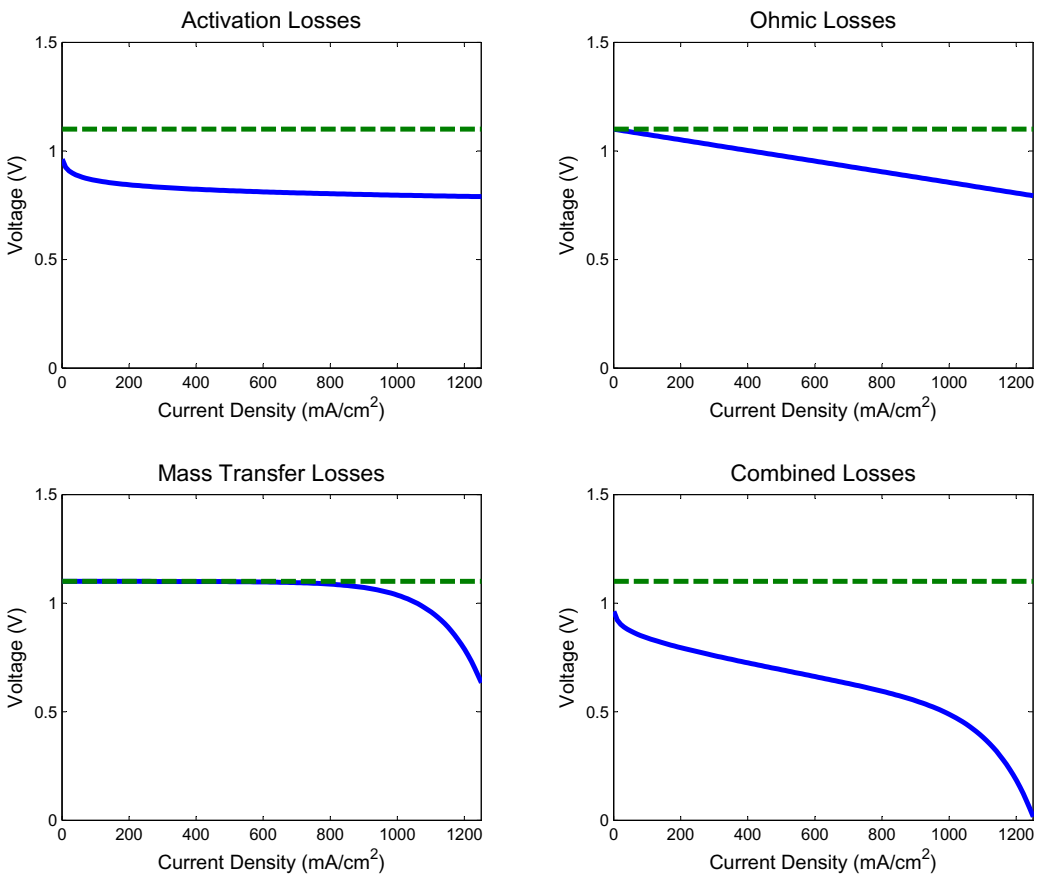


Figure 1.5: Polarization Curve Components and Their Cumulative Effect

| | | |
|---|---|---|
| where | $V$ | is the output voltage |
| | $E_0$ | is the open circuit voltage |
| | $\Delta V_{Activation}$ | is the voltage loss due to activation |
| | $\Delta V_{Ohmic}$ | is the voltage loss due to resistance |
| | $\Delta V_{MassTransport}$ | is the voltage loss due to reactant starvation |

**Open Circuit Voltage**

The theoretical energy available from a fuel cell is determined by 'Gibbs free energy.' This can be defined as, 'energy available to do external work, neglecting any work done

by changes in pressure and/or volume [1].' The chemical energy released is equal to the change in Gibbs free energy ($\Delta G_f$ in kJ).

For

$$\mathrm{H}_2 + \frac{1}{2}\mathrm{O}_2 \rightarrow \mathrm{H}_2\mathrm{O}$$

the change in specific Gibbs free energy $(\Delta \bar{g_f})$ in kJ/mol is given by

$$\Delta \bar{g_f} = \bar{g_f} \text{ of products} - \bar{g_f} \text{ of reactants} = (\bar{g_f})_{\mathrm{H_2O}} - (\bar{g_f})_{\mathrm{H_2}} - \frac{1}{2}(\bar{g_f})_{\mathrm{O_2}} \tag{1.5}$$

where $\bar{g_f}$ is the gibbs free energy per mole.

The change in Gibbs free energy depends on both temperature ($T_{fc}$) and pressure ($p$).

$$\Delta \bar{g_f} = \Delta \bar{g_f}^0 - \bar{R} T_{fc} \ln(\frac{p_{\mathrm{H_2}} p_{\mathrm{O_2}}^{\frac{1}{2}}}{p_{\mathrm{H_2O}}}) \tag{1.6}$$

It is known that two electrons complete the circuit for every water molecule that passes through the membrane. If $N_A$ is the Avagadro's Number, $2N_A$ electrons pass the circuit for every mole of hydrogen. If $-e$ is the charge of one electron, then

$$-2N_A e = -2F \tag{1.7}$$

where $F$ is the Faraday constant (electric charge per mole of electrons).

This determines the electrical work to move a charge around circuit.

$$\text{Electrical work done = charge} \times \text{ voltage} = -2FE \text{ joules}$$

where $E$ is the voltage of the fuel cell

If the system is completely reversible and experiences no losses, the electrical work is equal to the energy released. This is given by

$$\Delta \bar{g_f} = -2FE$$

which can be rearranged as

$$E = \frac{-\Delta \bar{g_f}}{2F} \tag{1.8}$$

This can be used to determine the open circuit voltage of a fuel cell at a specific operating temperature. For example, a hydrogen fuel cell operating at $80^\circ$ C has a $\Delta\bar{g_f} = -226.1$ kJ/mol resulting in an open circuit voltage of

$$E = \frac{226,100}{2 \times 96485} = 1.17\text{V} \tag{1.9}$$

**Losses**

A variety of losses exist in the fuel cell, and they dominate at different current densities. These losses include internal currents, fuel crossover, activation losses, ohmic losses, and mass transport losses. Internal currents and fuel crossover reduce the operational voltage even at open circuit conditions. Activation losses build quickly at low current densities. The ohmic losses are realized during operational range (when loaded). Mass transport losses are typically avoided due to their harmful effect on the MEA. The mass transport loss is seen at high current densities, but can occur whenever fuel cannot reach the MEA.

An internal current is the loss of an electron through the MEA. This means the electron is not used by load, but rather is conducted through the membrane. These are more significant in low temperature fuel cells (such as PEM). Fuel crossover is the leakage of hydrogen through the MEA without ionization. This is the diffusion of hydrogen across the membrane.

Activation losses (also called overvoltage or overpotential) is the voltage superimposed on the ideal voltage and applies to the difference generated at the electrode. The activation energy necessary to start the reaction towards the formation of water and electricity is the activation loss. This loss decreases with increased operational temperature [1].

Ohmic losses primarily caused by the electrolyte, the cell interconnects, and bipolar plates increase linearly with current density. The ohmic loss can be reduced by using electrodes with high conductivity, addressing the design of the bipolar plate, and by making the electrolyte as thin as possible. The ohmic loss is highly influenced by the humidification of the electrolyte. Proton conductivity improves with decreased distance between hydrophyllic regions. The hydrophyllic regions grow when they absorb water, reducing the distance between each other.

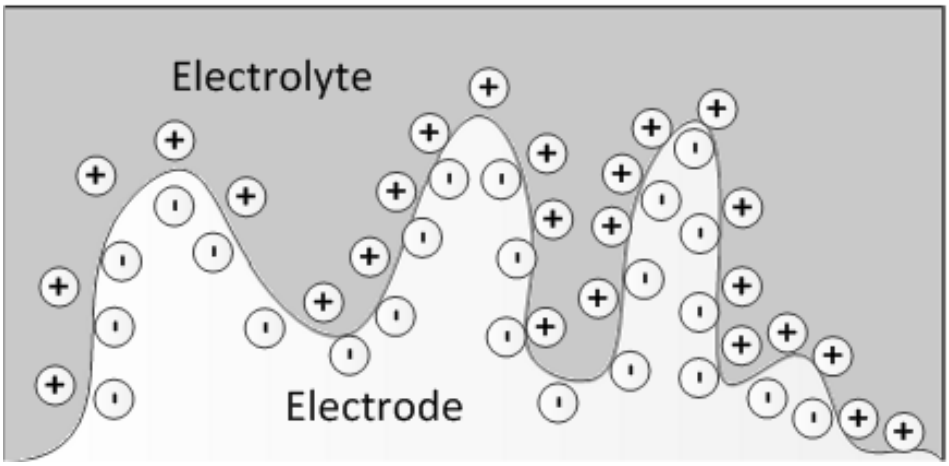


Figure 1.6: Charge Double Layer
at surface of fuel cell cathode

Mass transport losses occur when there is no longer a sufficient concentration of fuel or oxygen at the anode or cathode. This occurs when the fuel is being used faster than it can be supplied. These losses are responsible for the rapid voltage drop at high current densities [9]. Condensation within the flow channels can block hydrogen flow, creating an environment deprived of fuel.

This research focuses on activation loss and ohmic losses for classification purposes. These two losses are unavoidable in an automotive fuel cell, while mass transport losses are typically avoided by limiting the maximum current draw. An automotive fuel cell will deteoriate over time, or may even be damaged in production, and the identification of an issue may help prevent further damage through operation of the fuel cell.

**Charge Double Layer**

The charge double layer represented in Figure 1.6 is a phenomenon in which a build-up of charge occurs on the surfaces of two different materials in contact. The layer acts as a capacitor, when current increases charge increases and when current decreases charge decreases. This double layer effect gives an explanation for the activation overvoltage. The charge double layer must be present for a reaction to occur. It creates a high density of $H^+$ ions and electrons at the electrode/electrolyte interface. The chance of a reaction occuring

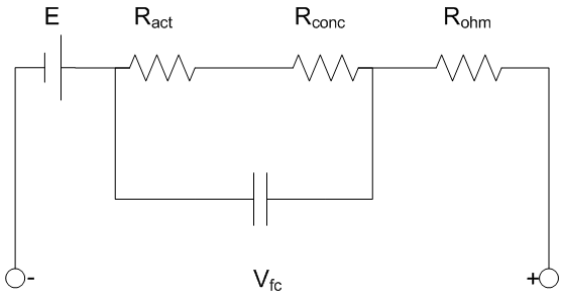


Figure 1.7: Fuel Cell Equivalent Circuit

depends on the density of the charge, electrons, and $H^+$ ions. Note: The charge double layer effect was ignored in Pukrushpan's model due to its fast transients. The dynamics are reported to be in the order of $10^{-19}$ seconds [4].

$$C\frac{dv_c}{dt} + \frac{v_c - v_0}{R_{act} + R_{conc}} = i \tag{1.10}$$

$$v_{fc} = E - v_c - iR_{ohm} \tag{1.11}$$

### 1.3.1 Recoverable Voltage Loss

#### Humidification

Humidification of a PEMFC is important for optimal efficiency [13]. The ability to carry protons improves as water is retained because the distance between hydrophillic sections decreases [1]. The oxidation reduction reaction generates $H_2O$ on the cathode side, naturally humidifying it. The anode does experience some humidification through this process. Protons moving through the aqueous environment of the MEA will carry water from the anode towards the cathode, this is called electro-osmotic drag.

The humidification on the anode side dries out without humidification of the hydrogen gas at higher loads [9]. At low loads back-diffusion will prevail to humidify the anode. It has been shown that a well hydrated membrane has up to 300 times more conductivity than a dry membrane. Low humidity not only increases resistance, but also minimizes access to reacting sites at the three-phase boundary layer, thus increasing activation losses as well as ohmic losses. Obviously, a wet membrane is preferred.

The accumulation of liquid water in the flow channels is just as detrimental. Flooding

hinders gas diffusion. In designs that incorporate parallel flows flooding will cause an unequal distribution of gas flow [14]. It has been observed that as water accumulates in the channels there is a slowly increasing voltage drop, and as the droplets aggregate to block reactants a rapid voltage drop is incurred.

**Contamination**

Contamination sources can come from either reactant gas, fuel cell stack components, or balance of plant equipment. Carbon monoxide (CO) is a major contaminant that can affect platinum (Pt) bonding sites[15, 16]. CO may come from impure fuel sources (particularly reformate) or from the air. CO from the air can crossover through the membrane. CO will occupy the reaction sites; it has higher kinetics and a slower reaction than hydrogen causing loss of efficiency. A single CO molecule can acquire two hydrogen bonding sites. Mitigation of CO can be achieved by running the fuel cell at higher operating temperatures or by running air/oxygen through the anode. Puffing air/oxygen through the anode can also reduce nitrogen dioxide $NO_2$ contamination (which is not catalyst related and fully reversible).

Fuel cell stack components can introduce contaminants to the membrane as well such as $Fe_3^+$, $Ni_2^+$, $Cu_2^+$, $Cr_3^+$, and Si. Deionized water from the coolant system can introduce Si, Al, S, K, Fe, Cu, Cl, V, and Cr. While the compressor (if a part of the system) can introduce a variety of oils.

**Nitrogen Build-Up**

Inert gases such as nitrogen ($N_2$) exist within $H_2$ stores. Nitrogen also permeates through the MEA from the cathode to the anode due to pressure differentials. As fuel is supplied to the anode a small supply of $N_2$ is released into the system. Dead-end anode systems are often used to improve $H_2$ utilization with periodic opening of an exhaust valve to purge the inert gases and water droplets [17]. The partial pressure of inert gases from the fuel source builds linearly with fuel usage. This decreases the partial pressure of $H_2$, thus increasing mass transport losses [18]. It can be difficult to optimize the timing of purging. Frequent

purging improves stack performance but increases parasitic losses, while low frequency purging increases the chance of water droplet formation of damage to the fuel cell. Adaptive controls based off of load requirements are best to achieve system stability and low system losses [19].

#### Transient Mass Transport Loss

Mass transport losses occur when the reactants drop in pressure on the surface of the electrodes. When $H_2$ or $O_2$ cannot be supplied quickly, a pressure drop occurs. During a transient, voltages may overshoot or undershoot the desired voltage. This can be a combination of the charge double layer effect and mass transfer effects [12]. A fuel cell cannot always supply the necessary power for the load, hence hybrid systems are developed.

### 1.3.2 Non-Recoverable Voltage Loss

Not all losses are recoverable or repairable. Throughout the life of a fuel cell it will experience damaging effects that degrade its performance. These can be exerted from mechanical forces or chemical reactions. An automotive fuel cell is exposed to a variety of potentially damaging chemicals from the atmosphere, it experiences shock and vibration from the road, and thermally cycles with each use. These losses may be repairable through refurbishment or replacement in a stack and their classification may extend the useful life of the fuel cell system.

#### Mechanical

Perforations, cracks, pin-holes, or tears can cause early failure in PEMFC life. Thermal cycling and humidity cycling cause mechanical stresses leading to MEA tears and pinholes. Fuel crossover occurs with the existence of a tear or hole in an MEA. This leads to a highly exothermic reaction between the reactants generating hot spots causing further degradation [20, 21, 14]. Thermal cycling can also lead to increased contact resistance between the membrane and electrodes. Increased contact resistance will increase the ohmic loss.

**Chemical/Electrochemical**

As shown earlier, chemical modifications of the catalyst layer can cause a degraded state of the fuel cell. Hydrogen sulfide and sulfur dioxide are contaminants that cause irreversible bonds on the Pt catalyst [15]. Besides contamination, the Pt activity sites may reduce in number. Pt particles detach from their carbon supports and dissolve in the electrolyte without redeposition. The Pt particles may also agglomerate by redepositing on existing Pt sites [16, 18]. This is called Ostwald Ripening.

The performance of Nafion is limited above $80^{\circ}$ Celcius. At high temperatures Nafion membranes decompose [20].

Fuel starvation causes the oxidation of the carbon supports [14]. The oxidation of carbon causes agglomeration of Pt particles, surface oxides CO and $CO_2$ form, and oxygen containing groups (carboxyl, carbonyl, hydroxyl, phenol, etc.) can be formed on the surface at high temperatures and/or high potentials [22]. Surface oxidation also increases hydrophilicity of the surface decreasing the gas permeability. Liquids fill the pores more easily and prevent gas transport. The oxidation causes an increase in electrode resistance by increasing the contact resistance.

These nonrecoverable losses at the activation and ohmic regions are a focus of this research. The ability to discriminate between recoverable and non-recoverable voltage is a goal and these must be modeled to create data for this activity.

## 1.4 Pattern Classification

Pattern classification is the assignment of a class or label based off of measurement(s). Some sort of sensory system takes these measurements. This system could be composed of thermometers, lasers, cameras, or other measurement devices. Fuel cell sensory measurements typically include stack coolant temperature, cathode inlet humidity, cathode/anode manifold pressures, cell and/or stack voltage, and stack current draw. These measurements are transformable by various pre-processing techniques. Features are extracted at this point.

These features are used to discriminate between classes using a variety of techniques ranging from support vector machines, neural networks, clustering, statistical methods, etc [23].

### 1.4.1 Fuel Cell Fault Recognition

Recent years have seen an increase in state of health (SOH) and fault recognition research [24]. State of health research is the analysis of remaining useful life (RUL) and fault recognition is the determination of the cause. This research tends to focus on determining fuel cell age, humidification, or balance of plant as seen in [25, 26, 27, 28]. Fault recognition is not easy in fuel cells due to the difficulty of discriminating faults. Fouquet *et al.* [29] shows this by presenting the polarization curve of a flooded membrane and a dry membrane overlapped. The curves are indistinguishable. Fouquet *et al.* determined that flooding and drying out can cause the same voltage drop.

Fouquet *et al.* used electrochemical impedance spectroscopy (EIS) measurements to effectively discriminate between flooded and dried cells. It is a technique that applies small currents to the fuel cell and returns frequency data. However, EIS measurements are time consuming, expensive, and difficult to implement in high power fuel cell systems.

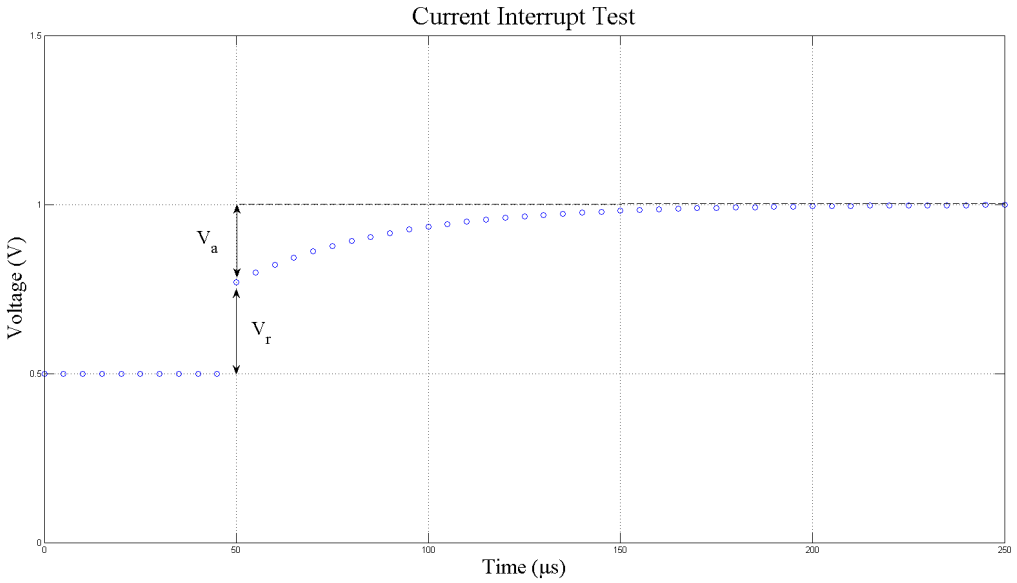


Figure 1.8: Current Interrupt Test

The current interupt (CI) technique is used to determine the ohmic drop in the fuel cell. Due to the capacitance effect discussed earlier, two voltage transients are seen when the current is interrupted [1]. Figure 1.8 shows an immediate change in voltage ($V_r$) due to the ohmic resistance, while a gradual change is due to the capacitance effect of the fuel cell. This method is difficult to apply in high power fuel cells and is inaccurate at low current densities [13].

Pressure drop across the cathode (where water is produced) can help determine flooding [30, 31]. An erratic voltage evolution due to the sudden evacuation of water can also determine a flooded state. This is difficult to employ in a fuel cell stack as pressure is not typically recorded on a cell by cell basis.

### 1.4.2 Classification

Previous studies used EIS measurements to determine fuel cell operating time. Onanena *et al.* [25] used feature extraction on a combination of EIS measurements and polarization curves to improve the FC operating time estimate. They show polarization curves vary with time. Their feature extraction on polarization curves estimated parameters for each polarization curve. Feature extraction on EIS measurements is achieved by plotting the real and imaginary portions separately.

Kim *et al.* [24] investigated state-of-health diagnosis with output voltage patterns and a hamming neural network. The output node states the relative health of the cell, ranging from zero to one. No fault classification is determined. Steiner *et al.* [26] introduced a novel approach to determining hydration from the voltage transients by applying the wavelet transformation. Two features are extracted from the wavelet decomposition to effectively discriminate between flooding and no flooding. The algorithm was trained and tested on collected data and did not work for real-time diagnosis. Steiner *et al.* [27] explored neural network modeling to discriminate flooding and modeling using voltage, pressure drop, current, stack temperatures, and air flow rate. The neural network discriminated flooding and dry states successfully.

## 1.5 Proposed Research

The proposed thesis improves the automotive fuel cell model developed by Pukrushpan *et al.* [3, 4] of the University of Michigan. The proposed thesis continues by using the enhanced automotive fuel cell model to develop fuel cell fault classification techniques. Pukrushpan developed a model for control theory and did not include system responses to transients beside reactant gases in his scope of work.

This research includes the development of multi-cell deviation by simulating an additional cell in parallel with the fuel cell stack. The additional cell allows for seeded fault testing without significantly affecting stack dynamics. A thermal model is developed to track fuel cell temperature in response to changing current draw. The thermal model neglects anode and cathode convection and convection external to the fuel cell stack assembly. Humidification controls are implemented to maintain a set cathode outlet humidity by controlling the thermal model. Nitrogen permeation across the membrane is incorporated for its effect on voltage, oxygen permeation and hydrogen permeation are neglected. An anode manifold is developed as an outlet flow path for anode gases, and an anode purging control system is implemented to maintain a set hydrogen mole fraction. Each of these changes create transients that will impact the fuel cell stack voltage.

The enhanced automotive fuel cell model is used to generate data for the development of fault classification techniques. A polarization curve test is applied to the enhanced automotive fuel cell model to study its state of health. Seeded faults are applied to the deviated cell to modify its activation losses and ohmic losses. The effectiveness of a Naïve Bayes classifier in determining the fuel cell state of health is studied. Principal component analysis and independent component analysis are investigated for their effectiveness as preprocessing tools for the Naïve Bayes classifier.

# Chapter 2

# Fuel Cell System Model

## 2.1 Fuel Cell Model

Pukrushpan *et al.* [9] developed an automotive fuel cell system for studying control strategies, particularly in regards to reactant gases. This model expands on the voltage model developed by Amphlett *et al.* [32]. This model is used because it is well accepted in literature; it is found in many journals as the starting point of additional research. Pukrushpan *et al.* used data from the FORD P2000 at the Ford Research Laboratory to validate his model. A review of the automotive fuel cell model is given in this chapter, for a more in depth analysis see [9]. The model is idealized and lacks important real world effects. These include a lack of cell to cell deviation (as one cell is modeled and multiplied by $N_{fc}$ to create a stack), no thermal dynamics, and no effects from impurities in the fuel and air.

### 2.1.1 Fuel Cell Voltage

Fuel cell operating voltage is a function of many things: temperature, pressure, and humidification to name a few. The three well documented losses are activation loss, ohmic loss, and concentration loss. Each loss is discussed and then combined with the reversible open circuit voltage in this section to create the voltage model.

The reversible open circuit voltage (also known as "Nernst Voltage") is the theoretical maximum voltage of a fuel cell. The basis of this calculation comes from the gibbs free energy analysis seen in the previous chapter. At standard temperature and pressure the maximum open circuit voltage is 1.229 volts. As temperature or pressure changes so does the reversible open circuit voltage ($E$).

$$E = 1.229 - 0.85 \times 10^{-3}(T_{fc} - 298.15) + 4.3085 \times 10^{-5} T_{fc}[ln(p_{H_2} + \frac{1}{2} ln(p_{O_2})] \quad (2.1)$$

where $T_{fc}$ is the fuel cell temperature in Kelvin, pressure of hydrogen ($p_{H_2}$) and oxygen ($p_{O_2}$) are expressed in atm. The reversible open circuit voltage cannot be maintained during the fuel cell's operation. The fuel cell's terminal voltage during operation is a combination of the open circuit voltage and the following losses.

Activation loss ($v_{act}$) is typically determined with the Tafel equation,

$$v_{act} = a \ln(\frac{i}{i_0}) \quad (2.2)$$

where $i$ is the cell current density and $i_0$ is the exchange current density [1]. However, since the Tafel equation is only valid for current densities greater than the exchange current density ($i > i_0$), a new model is required. Eq. (2.3) is derived empirically,

$$v_{act} = v_0 + v_a(1 - e^{-c_1 i}) \quad (2.3)$$

with the values of voltage drop at zero current density ($v_0$) and constants $v_a$ and $c_1$ determined from data fits to Ford fuel cell data.

The ohmic loss ($v_{ohm}$) is a function of resistance ($R_{ohm}$) and current ($i$),

$$v_{ohm} = iR_{ohm} \quad (2.4)$$

where the resistance incorporates the electrodes, the membrane, and the various fuel cell stack components. Membrane humidification changes the ion conductivity of the membrane, so resistance becomes a function of humidification and temperature.

$$R_{ohm} = \frac{t_m}{\sigma_m} \quad (2.5)$$

where $t_m$ is membrane thickness and $\sigma_m$ is a function of membrane water content ($\lambda_m$) and fuel cell temperature ($T_{fc}$)

$$\sigma_m = b_1 e^{b_2(\frac{1}{303} - \frac{1}{T_{fc}})} \quad (2.6)$$

where $b_2$ is a constant and $b_1$ is a function of $\lambda_m$,

$$b_1 = b_{11}\lambda_m - b_{12} \tag{2.7}$$

with $b_{11}$ and $b_{12}$ as empirically determined constants.

The rapid voltage loss at high current densities is due to mass transport losses, also known as concentration loss ($v_{conc}$). Hydrogen cannot access the activity sites as quickly as current is drawn. This is governed by:

$$v_{conc} = i(c_2\frac{i}{i_{max}})^{c_3} \tag{2.8}$$

where $c_2$, $c_3$, and $i_{max}$ are constants that depend on the reactant partial pressures and the temperature. Eq. (2.9) shows the combined losses used in determining the operating voltage. This equation can be used to generate a polarization curve.

$$V = E - [v_0 + v_a(1 - e^{-c_1 i})] - [iR_{ohm}] - [i(c_2\frac{i}{i_{max}})^{c_3}] \tag{2.9}$$

The constant values for fuel cell terminal voltage are determined with parameter estimation techniques to Ballard fuel cell data [32].

$$\begin{aligned} E = {} & 1.229 - 8.5 * 10^{-4}(T_{fc} - 298.15) \\ & + 5.308 * 10^{-5}T_{fc}[ln(\frac{p_{H_2}}{1.01325}) + \frac{1}{2}\ln(\frac{p_{O_2}}{1.01325})] \end{aligned} \tag{2.10}$$

$$\begin{aligned} v_0 = {} & 0.279 - 8.5 + 10^{-4}(T_{fc} - 298.15) \\ & + 4.308 * 10^{-5}[\ln(\frac{p_{ca} - p_{sat}}{1.01325}) - \frac{1}{2}\ln(\frac{0.1173(p_{ca} - p_{sat})}{1.01325}) \end{aligned} \tag{2.11}$$

$$\begin{aligned} v_a = {} & (-1.618 * 10^{-5}(T_{fc} + 1.618 * 10^{-2})(\frac{p_{O_2}}{0.1173} + p_{sat})^2 \\ & + (1.8 * 10^{-4}T_{fc} - 0.166)(\frac{p_{O_2}}{0.1173} + p_{sat}) + (-5.8 * 10^{-4}T_{fc} + 0.5736) \end{aligned} \tag{2.12}$$

$$
\begin{aligned}
c_1 &= 10 \\
c_3 &= 2 \\
t_m &= 0.0125 \\
i_{max} &= 2.2 \\
b_{11} &= 0.005139 \\
b_{12} &= 0.00326 \\
b_2 &= 350
\end{aligned}
$$

$$
c_2 = \begin{cases}
(7.16 * 10^{-4} T_{fc} - 0.622)(\frac{p_{O_2}}{0.1173} + p_{sat}) & \\
\qquad +(-1.45 * 10^{-3} T_{fc} + 1.68 & \text{for } (\frac{p_{O_2}}{0.1173} + p_{sat}) < 2 \text{ atm} \\
(8.66 * 10^{-5} T_{fc} - 0.068)(\frac{p_{O_2}}{0.1173} + p_{sat}) & \\
\qquad +(-1.60 * 10^{-4} T_{fc} + 0.54 & \text{for } (\frac{p_{O_2}}{0.1173} + p_{sat}) \geq 2 \text{ atm}
\end{cases}
$$

### 2.1.2 Reactant Flow

Reactant flow is modeled using the principles of mass conservation, psychrometrics, and thermodynamics. All gases are assumed to behave as ideal gases. All outlet measurements are assumed to be uniform throughout the stack. All flows denoted with a $\dot{m}$ have the units kg/sec. The subscripts $c$ and $a$ refer to the cathode and anode respectively. Inlet flows use the subscript $i$ and outlet flows use $o$. The following is a recreation of the equations used by Pukrushpan *et al.* for the automotive fuel cell model. For more detail please see [9].

Below, some key variables are defined.

$\dot{m}$ refers to mass flow rate in kg/sec

$T$ refers to temperature in degrees Kelvin

$P$ refers to pressure in Pascals

$\phi$ refers to relative humidity, a ratio from $0$ to $1$

$y$ refers to a mole fraction, a ratio from $0$ to $1$

$x$ refers to a mass fraction, a ratio from $0$ to $1$

$M$ refers to Molar mass in g/mol

$m$ refers to mass in kg

$V$ refers to volume

$R$ refers to gas constants

**Cathode**

The cathode model takes the inputs of stack current ($I_{st}$), stack temperature ($T_{st}$), water flow across the membrane ($\dot{m}_{v,membr}$), downstream pressure ($p_{rm}$), and inlet flow properties such as temperature ($T_{c,i}$), pressure ($p_{c,i}$), mass flow rate ($\dot{m}_{c,i}$), humidity ($\phi_{c,i}$), and oxygen mole fraction ($y_{\mathrm{O}_2,c,i}$). The cathode and anode are each treated as one volume. Perfect mixing is assumed thus the outlet variables are equivalent to the stack variables for temperature, pressure, humidity, and oxygen mole fraction.

Three state equations are developed by mass conservation at the cathode.

$$\frac{dm_{\mathrm{O}_2,ca}}{dt} = \dot{m}_{\mathrm{O}_2,c,i} - \dot{m}_{\mathrm{O}_2,c,o} - \dot{m}_{\mathrm{O}_2,rx} \tag{2.13}$$

$$\frac{dm_{\mathrm{N}_2,ca}}{dt} = \dot{m}_{\mathrm{N}_2,c,i} - \dot{m}_{\mathrm{N}_2,c,o} \tag{2.14}$$

$$\frac{dm_{w,ca}}{dt} = \dot{m}_{v,c,i} - \dot{m}_{v,c,o} + \dot{m}_{v,c,gen} + \dot{m}_{v,membr} + \dot{m}_{l,c,o} \tag{2.15}$$

Where $\dot{m}_{\mathrm{O}_2,c,i}$ is the mass flow rate of oxygen gas entering the cathode

$\dot{m}_{\mathrm{O}_2,c,o}$ is the mass flow rate of oxygen gas leaving the cathode

$\dot{m}_{\mathrm{O}_2,rx}$ is the rate of oxygen reacted

$\dot{m}_{\mathrm{N}_2,c,i}$ is the mass flow rate of nitrogen gas entering the cathode

$\dot{m}_{\mathrm{N}_2,c,o}$ is the mass flow rate of nitrogen gas leaving the cathode

$\dot{m}_{v,c,i}$ is the mass flow rate of vapor entering the cathode

$\dot{m}_{v,c,o}$ is the mass flow rate of vapor leaving the cathode

$\dot{m}_{v,c,gen}$ is the rate of vapor generated in the fuel cell reaction

$\dot{m}_{v,membr}$ is the mass flow rate of water transfer across the membrane

$\dot{m}_{l,c,o}$ is the rate of liquid water leaving the cathode

The maximum mass of vapor ($m_{v,max,ca}$) held in the cathode volume can be calculated with

$$m_{v,max,ca} = \frac{p_{sat} V_{ca}}{R_v T_{st}} \tag{2.16}$$

If the mass of the water calculated in Eq. 2.15 is greater than the maximum mass of vapor the gas can hold the mass of vapor and liquid are calculated by:

$$m_{v,ca} = m_{v,max,ca} \tag{2.17}$$

$$m_{l,ca} = m_{w,ca} - m_{v,max,ca} \tag{2.18}$$

else, the mass of liquid water is equal to zero and $m_{v,ca} = m_{w,ca}$.

The pressure and relative humidity of the gas inside the cathode can be determined using the masses of oxygen, nitrogen, stack temperature, pressure, and vapor. Oxygen, nitrogen, and vapor partial pressures are determined from the masses currently in the system.

Oxygen partial pressure:

$$p_{\mathrm{O}_2,ca} = \frac{m_{\mathrm{O}_2,ca} R_{\mathrm{O}_2} T_{st}}{V_{ca}} \tag{2.19}$$

Nitrogen partial pressure:

$$p_{\mathrm{N}_2,ca} = \frac{m_{\mathrm{N}_2,ca} R_{\mathrm{N}_2} T_{st}}{V_{ca}} \tag{2.20}$$

Vapor partial pressure:

$$p_{v,ca} = \frac{m_{v,ca} R_v T_{st}}{V_{ca}} \tag{2.21}$$

Partial pressure of dry air:

$$p_{air,ca} = p_{\mathrm{O}_2,ca} + p_{\mathrm{N}_2,ca} \tag{2.22}$$

Cathode pressure:

$$p_c = p_{air,c} + p_{v,c} \tag{2.23}$$

Oxygen mole fraction:

$$y_{\mathrm{O}_2,c} = \frac{p_{\mathrm{O}_2,ca}}{p_{air,c}} \tag{2.24}$$

Relative humidity:

$$\phi_{ca} = \frac{p_{v,ca}}{p_{sat} T_{st}} \tag{2.25}$$

Vapor pressure:

$$p_{v,c,i} = \phi_{c,i} p_{sat} T_{c,i} \tag{2.26}$$

Dry air partial pressure:

$$p_{air,c,i} = p_{c,i} - p_{v,c,i} \tag{2.27}$$

Humidity ratio:

$$\omega_{c,i} = \frac{M_v}{M_{air,c,i}} \frac{p_{v,c,i}}{p_{air,c,i}} \tag{2.28}$$

Air molar mass:

$$M_{air,c,i} = y_{O_2,c,i} M_{O_2} + (1 - y_{O_2,c,i}) M_{N_2} \tag{2.29}$$

Dry air mass flow rate:

$$\dot{m}_{air,c,i} = \frac{1}{1 + \omega_{c,i}} \dot{m}_{c,i} \tag{2.30}$$

Vapor flow rate:

$$\dot{m}_{v,c,i} = \dot{m}_{c,i} - \dot{m}_{air,c,i} \tag{2.31}$$

Oxygen mass flow rate:

$$\dot{m}_{\mathrm{O}_2,c,i} = x_{\mathrm{O}_2,c,i} \dot{m}_{air,c,i} \tag{2.32}$$

Nitrogen mass flow rate:

$$\dot{m}_{\mathrm{N}_2,c,i} = (1 - x_{\mathrm{O}_2,c,i}) \dot{m}_{air,c,i} \tag{2.33}$$

Oxygen mass fraction:

$$x_{\mathrm{O}_2,c,i} = \frac{m_{\mathrm{O}_2}}{m_{dryair}} = \frac{y_{\mathrm{O}_2,c,i}\dot{m}_{air,c,i}}{y_{\mathrm{O}_2,c,i}M_{\mathrm{O}_2} + (1 - y_{\mathrm{O}_2,c,i})M_{\mathrm{N}_2}} \tag{2.34}$$

A simplified orifice equation is used to determine cathode mass flow rate out

$$\dot{m}_{c,o} = k_{c,o}(p_{ca} - p_{rm}) \tag{2.35}$$

The following equations are used to determine the cathode outlet flows.

$$M_{air,c} = y_{\mathrm{O}_2,ca}M_{\mathrm{O}_2} + (1 - y_{\mathrm{O}_2,c})M_{\mathrm{N}_2} \tag{2.36a}$$

$$\omega_{c,i} = \frac{M_v}{M_{air,c}}\frac{p_{v,ca}}{p_{air,c}} \tag{2.36b}$$

$$\dot{m}_{air,c,o} = \frac{1}{1 + \omega_{c,o}}\dot{m}_{c,o} \tag{2.36c}$$

$$\dot{m}_{v,c,o} = \dot{m}_{c,o} - \dot{m}_{air,c,o} \tag{2.36d}$$

$$x_{\mathrm{O}_2,c,i} = \frac{m_{\mathrm{O}_2}}{m_{dryair}} = \frac{y_{\mathrm{O}_2,c,i}\dot{m}_{air,c,i}}{y_{\mathrm{O}_2,c,i}M_{\mathrm{O}_2} + (1 - y_{\mathrm{O}_2,c,i})M_{\mathrm{N}_2}} \tag{2.36e}$$

$$\dot{m}_{\mathrm{O}_2,c,o} = x_{\mathrm{O}_2,ca}\dot{m}_{air,c,o} \tag{2.36f}$$

$$\dot{m}_{\mathrm{N}_2,c,o} = (1 - x_{\mathrm{O}_2,ca})\dot{m}_{air,c,o} \tag{2.36g}$$

The amount of vapor generated ($\dot{m}_{v,ca,gen}$) and the amount of oxygen reacted ($\dot{m}_{\mathrm{O}_2,rx}$) are calculated as a function of current. For oxygen usage, it is known that four electrons are transfered for each mole of oxygen.

$$\text{charge} = 4F \times \text{amount of } \mathrm{O}_2 \tag{2.37}$$

where $F$ is farads. If we rearrange for $\mathrm{O}_2$ and divide by time,

$$\mathrm{O}_2 \text{ usage } = \frac{I}{4F}\text{moles s}^{-1} \tag{2.38}$$

then convert from moles/sec to to kg/sec and multiply by $N_{fc}$ cells for a stack, we achieve

$$\dot{m}_{\mathrm{O}_2,rx} = M_{\mathrm{O}_2}\frac{N_{fc}I_{st}}{4F} \tag{2.39}$$

This same process can be followed for water production, but per equation 1.3 only 2 electrons are involved per mole of $H_2O$.

$$\dot{m}_{v,ca,gen} = M_v \frac{N_{fc} I_{st}}{2F} \tag{2.40}$$

**Anode Flow**

Two state equations are developed by mass conservation for the anode.

$$\frac{dm_{\mathrm{H}_2,an}}{dt} = \dot{m}_{\mathrm{H}_2,a,i} - \dot{m}_{\mathrm{H}_2,a,o} - \dot{m}_{\mathrm{H}_2,rx} \tag{2.41}$$

$$\frac{dm_{w,ca}}{dt} = \dot{m}_{v,a,i} - \dot{m}_{v,a,o} - \dot{m}_{v,membr} - \dot{m}_{l,a,o} \tag{2.42}$$

Where $\dot{m}_{\mathrm{H}_2,c,i}$ is the mass flow rate of hydrogen gas entering the anode

$\dot{m}_{\mathrm{H}_2,c,o}$ is the mass flow rate of hydrogen gas leaving the anode

$\dot{m}_{\mathrm{H}_2,rx}$ is the rate of hydrogen reacted

$\dot{m}_{v,a,i}$ is the mass flow rate of vapor entering the anode

$\dot{m}_{v,a,o}$ is the mass flow rate of vapor leaving the anode

$\dot{m}_{v,membr}$ is the mass flow rate of water transfer across the membrane

$\dot{m}_{l,a,o}$ is the rate of liquid water leaving the anode

The maximum mass of vapor held in the anode volume can be calculated with

$$m_{v,max,an} = \frac{p_{sat} V_{an}}{R_v T_{st}} \tag{2.43}$$

If the mass of the water calculated in Eq. 2.42 is greater than the maximum mass of vapor the gas can hold the mass of vapor and liquid are calculated by:

$$m_{v,an} = m_{v,max,an} \tag{2.44}$$

$$m_{l,an} = m_{w,an} - m_{v,max,an} \tag{2.45}$$

else, the mass of liquid water is equal to zero and $m_{v,an} = m_{w,an}$.

Hydrogen partial presure in anode:

$$p_{\mathrm{H}_2,an} = \frac{m_{\mathrm{H}_2,an} R_{\mathrm{H}_2} T_{st}}{V_{an}} \tag{2.46}$$

Vapor partial pressure:

$$p_{v,an} = \frac{m_{v,an} R_v T_{st}}{V_{an}} \tag{2.47}$$

Anode pressure:

$$p_{an} = p_{\mathrm{H}_2,an} + p_{v,an} \tag{2.48}$$

Relative Humidity:

$$\phi_{an} = \frac{p_{v,an}}{p_{sat} T_{st}} \tag{2.49}$$

Vapor pressure:

$$p_{v,a,i} = \phi_{a,i} p_{sat} T_{a,i} \tag{2.50}$$

Hydrogen partial pressure at anode inlet:

$$p_{\mathrm{H}_2,a,i} = p_{a,i} - p_{v,a,i} \tag{2.51}$$

Anode humidity ratio:

$$\omega_{a,i} = \frac{M_v}{M_{\mathrm{H}_2}} \frac{p_{v,an}}{p_{a,an}} \tag{2.52}$$

Flow rates of hydrogen and vapor:

$$\dot{m}_{\mathrm{H}_2,a,i} = \frac{1}{1 + \omega_{a,i}} \dot{m}_{a,i} \tag{2.53}$$

$$\dot{m}_{v,a,i} = \dot{m}_{a,i} - \dot{m}_{\mathrm{H}_2,a,i} \tag{2.54}$$

Derived from equation 1.2 the mass flow rate of $\mathrm{H}_2$ can be determined:

$$\dot{m}_{\mathrm{H}_2,rx} = M_{\mathrm{H}_2} \frac{N_{fc} I}{2F} \tag{2.55}$$

If an anode purge rate is known, hydrogen and vapor mass flow rate are given by:

$$\dot{m}_{\mathrm{H}_2,a,o} = \frac{1}{1 + \omega_{a,o}} \dot{m}_{a,o} \tag{2.56}$$

$$\dot{m}_{v,a,o} = \dot{m}_{a,o} - \dot{m}_{\mathrm{H}_2,a,o} \tag{2.57}$$

where

$$\omega_{a,o} = \frac{M_v}{M_{\mathrm{H}_2}} \frac{p_{v,an}}{p_{\mathrm{H}_2,ca}} \tag{2.58}$$

### 2.1.3 Membrane Hydration

The membrane hydration model determines the water content in the membrane and the rate of water mass flow ($N$) across the membrane. The model does not account for mass transfer of nitrogen or other contaminants. Uniform water content and mass flow are assumed across the membrane. Both are functions of stack current and relative humidity inside the anode and cathode flow channels.

Two phenomena are involved in the transport of water across the membrane. Electro-osmotic drag by the $H^+$ ions brings water from the anode to cathode. $N_{v,osmotic}$ in mol/(sec*cm$^2$) is the net water flow from anode to cathode due to electro-osmotic drag.

$$N_{v,osmotic} = n_d \frac{i}{F} \tag{2.59}$$

where $i$ (A/cm$^2$) is the stack current density.

Back-diffusion of water from the cathode to the anode occurs due to the difference in humidity across the membrane. The membrane water concentration gradient is assumed to be linear. The net water flow from cathode to anode due to back diffusion ($N_{v,diff}$) is shown.

$$N_{v,diff} = n_d \frac{dc_v}{dy} \tag{2.60}$$

where $c_v$ (mol/cm$^3$) is the water concentration, $y$ (cm) is the distance in the direction normal to the membrane, and $D_w$ (cm$^2$/sec) is the diffusion coefficient of water in the membrane.

Combining the two equations, assuming positive flow from anode to cathode and a linear water coefficient gradient, gives us the net flow of water ($N_{v,membr}$) in mol/(sec*cm$^2$).

$$N_{v,membr} = n_d \frac{i}{F} - D_w \frac{(c_{v,ca} - c_{v,an})}{t_m} \tag{2.61}$$

This can be used to determine the the total stack mass flow rate across the membrane.

$$\dot{m}_{v,membr} = N_{v,membr} \times M_v \times A_{fc} \times N_{fc} \tag{2.62}$$

where $M_v$ is the vapor molar mass, $A_{fc}$ (cm$^2$) is the fuel cell active area, and $N_{fc}$ is the number of cells in the stack.

## 2.2 Balance of Plant

The balance of plant created by Pukrushpan *et al.* consists of everything that supports the fuel cell stack. This includes the air compressor, the air cooler, piping (inlet and outlet manifolds), and the humidification system. Stack thermal transients and the cooling system are ignored by Pukrushpan for their slower transients. The various accessories can be seen in Figure 2.1.

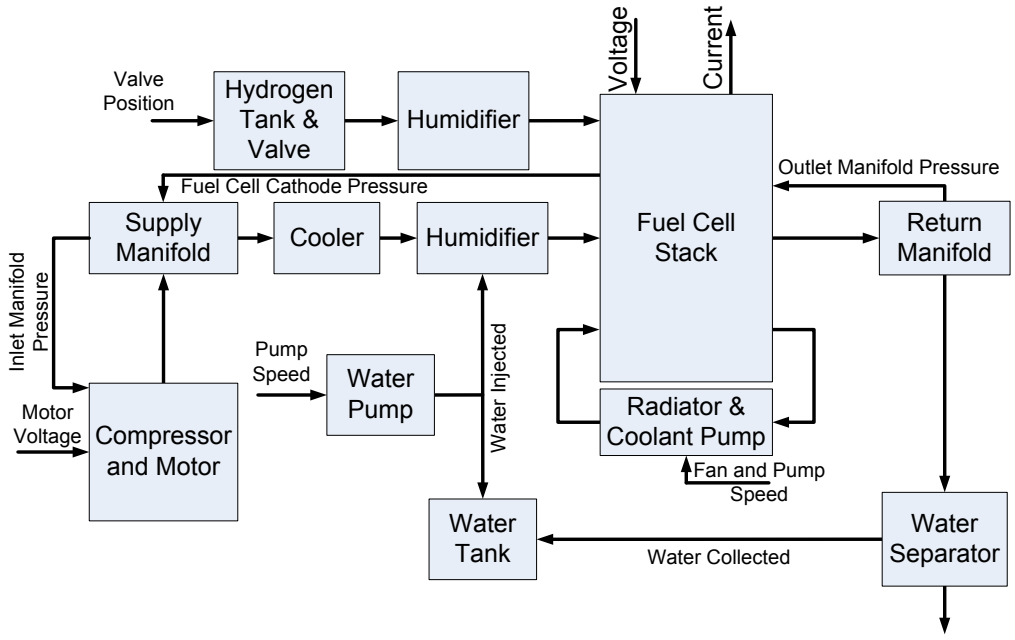


Figure 2.1: System Block Diagram (Recreated from [9])

The compressor model is built in two parts. The first is a compressor map to determine air flow rate, exit temperature, and required compressor power. The second part represents compressor and motor inertia to define compressor speed. The inputs include air pressure ($p_{cp,i}$), air temperature ($T_{cp,i}$), voltage command ($v_{cm}$), and downstream pressure ($p_{cp,out}$). Inlet air is assumed atmospheric and $25^\circ$ C. The normalized compressor flow rate ($\Phi$) is given by

$$\Phi = \Phi_{max}[1 - \exp(\beta(\frac{\psi}{\psi_{max}} - 1))] \tag{2.63}$$

where the Jensen and Kristensen method is used to determine the dimensionless head parameter $\psi$.

$$\psi = C_p T_{cp,i}[(\frac{p_{cp,o}}{p_{cp,i}})^{\frac{\gamma-1}{\gamma}} - 1]/(\frac{U_{cp}^2}{2}) \tag{2.64}$$

$T_{cp,i}$ is the air inlet temperature in Kelvin, $\gamma$ is the ratio of specific heats at constant pressure ($C_p/C_v$), and the compressor blade tip speed $U_{cp}$ is given by

$$U_{cp} = \frac{\pi}{60} d_c N_{cr} \tag{2.65}$$

where $d_c$ is the compressor diameter (0.2286 m) and $N_{cr}$ is the corrected compressor speed (rpm). The corrected compressor speed is equivalent to the compressor speed (rpm), $N_{cr} = N_{cp}/\sqrt{\theta}$ where the corrected temperature $\theta = T_{cp,i}/288$ Kelvin. The variables $\phi_{max}$, $\beta$, and $\psi_{max}$ are functions of the Mach number ($Ma$).

$$\phi_{max} = a_4 Ma^4 + a_3 Ma^3 + a_2 Ma^2 + a_1 Ma + a_0 \tag{2.66}$$

$$\beta = b_2 Ma^2 + b_1 Ma + b_0 \tag{2.67}$$

$$\psi_{max} = ci_5 Ma^5 + c_4 Ma^4 + c_3 Ma^3 + c_2 Ma^2 + c_1 Ma + c_0 \tag{2.68}$$

The Mach number can be solved by

$$Ma = \frac{U_{cp}}{\sqrt{\gamma R_{air} T_{cp,i}}} \tag{2.69}$$

where the air gas constant $R_{air} = 286.9$ J/(kg K). This is all used to determine the mass flow rate of air ($\dot{m}_{cr}$) in kg/sec

$$\dot{m}_{cr} = \phi \rho_{air} \frac{\pi}{4} d_c^2 U_{cp} \tag{2.70}$$

The compressor outlet temperature $T_{cp,o}$ is calculated by

$$T_{cp,o} = T_{cp,i} + \frac{T_{cp,i}}{\eta_{cp}}[(\frac{p_{cp,o}}{p_{cp,i}})^{\frac{\gamma-1}{\gamma}} - 1] = T_{atm} + \frac{T_{atm}}{\eta_{cp}}[(\frac{p_{sm}}{p_{atm}})^{\frac{\gamma-1}{\gamma}} - 1] \tag{2.71}$$

where the efficiency of the compressor $\eta_{cp}$ is determined from a look up table based off the mass flow rate and pressure ratio across the compressor. The compressor drive torque ($\tau_{cp}$)

in N-m is found with

$$\tau_{cp} = \frac{C_p T_{atm}}{\omega_{cp}\eta_{cp}}[(\frac{p_{sm}}{p_{atm}})^{\frac{\gamma-1}{\gamma}} - 1]\dot{m}_{cp} \tag{2.72}$$

where $C_p$ is the specific heat capacity of air in J/(kg K) and $\gamma$ is the ratio of specific heats of air. This torque is used in a lumped rotational model of the compressor and motor.

$$J_{cp}\frac{d\omega_{cp}}{dt} = \tau_{cm} - \tau_{cp} \tag{2.73}$$

where $J_{cp}$ is inertia of both the compressor and motor in kg m$^2$, $\omega_{cp}$ is the compressor speed in rad/sec, $T_{cm}$ and $T_{cp}$ are the compressor motor torque input and the torque required to drive the compressor in N-m. A static motor equation is used to determine the compressor motor torque ($\tau_{cm}$).

$$\tau_{cm} = \eta_{cm}\frac{k_t}{T_{cm}}(v_{cm} - k_v\omega_{cp}) \tag{2.74}$$

where $k_t$, $k_v$, and $R_{cm}$ are motor constants and $\eta_{cm}$ is the mechanical efficiency of the motor.

Manifold dynamics represent the inlet manifold and outlet manifolds. The inlet manifold comprises the volumes of pipes between the compressor and the fuel cell stack, including the volume of the air cooler and humidifier. The return manifold represents the volume of the fuel cell stack exhaust. Each manifold follows the conservation of mass principle.

$$\frac{dm}{dt} = \dot{m}_i - \dot{m}_o \tag{2.75}$$

where $m$ is the mass in the manifold, $\dot{m}_i$ represents the mass flow rate in, and $\dot{m}_o$ represents the mass flow rate out. The inlet manifold is not assumed to be isothermal, thus $T \neq T_i$. The manifold pressure is modeled by

$$\frac{\gamma R_a}{V}(\dot{m}_i T_i - \dot{m}_o T_o) \tag{2.76}$$

The manifold outlet flow is governed by a two part nozzle equation that is dependent on the critical pressure ratio:

$$\frac{p_2}{p_{1\,crit}} = (\frac{2}{\gamma+1})^{\frac{\gamma}{\gamma-1}} \tag{2.77}$$

If the pressure drop is less than the critical pressure, the flow is subcritical and governed by

$$\dot{m} = \frac{C_D A_T p_1}{\sqrt{\bar{R} T_1}} (\frac{p_2}{p_1})^{\frac{1}{\gamma}} [\frac{2\gamma}{\gamma - 1} [1 - (\frac{p_2}{p_1})^{\frac{\gamma-1}{\gamma}}]]^{\frac{1}{2}} \tag{2.78}$$

while critical flow is determined by

$$\dot{m} = \frac{C_D A_T p_1}{\sqrt{\bar{R} T_1}} \gamma^{\frac{1}{2}} (\frac{2}{\gamma + 1})^{\frac{\gamma+1}{2(\gamma-1)}} \tag{2.79}$$

where $C_D$ is the discharge coefficient of the nozzle, $A_T$ is the nozzle opening ($m^2$), and $\bar{R}$ is the universal gas constant. But when the pressure drop is relatively small, a linearized form can be calculated for subcritical nozzle flow. This nozzle outlet flow $\dot{m}$ is given by

$$\dot{m} = k(p_1 - p_2) \tag{2.80}$$

where $k$ is the nozzle constant.

The supply manifold has a relatively small pressure drop between the manifold and the cathode, so a linearized form is used for the supply manifold's outlet mass flow ($\dot{m}_{sm,o}$).

$$\dot{m}_{sm,o} = k_{sm,o}(p_{sm} - p_c) \tag{2.81}$$

where $p_{sm}$ is the supply manifold pressure, $p_{ca}$ is the cathode pressure, and $k_{sm,o}$ is the supply manifold outlet flow constant. The temperature is expected to drop in the supply manifold since the air compressor outlet temperature is assumed to be high. Thus the following equations model the supply manifold.

$$\frac{dm_{sm}}{dt} = \dot{m}_{cp} - \dot{m}_{sm,o} \tag{2.82}$$

$$\frac{dp_{sm}}{dt} = \frac{\gamma R_{air}}{V_{sm}} (\dot{m}_{cp} T_{cp,o} - \dot{m}_{sm,o} T_{sm}) \tag{2.83}$$

where $V_{sm}$ is the supply manifold volume and $T_{sm}$ is the supply manifold temperature. The return manifold however, has a small temperature change and a large pressure drop. This is the opposite of the inlet manifold. As such the return manifold pressure is modeled with

$$\frac{dp_{rm}}{dt} = \frac{R_{air} T_{rm}}{V_{rm}} (\dot{m}_{c,o} - \dot{m}_{rm,o}) \tag{2.84}$$

where $T_{rm}$ is the return manifold temperature and $V_{rm}$ is the return manifold volume. The nonlinear nozzle equation for subcritical flow is given by

$$\dot{m}_{rm,o} = \frac{C_{D,rm} A_{T,rm} p_{rm}}{\sqrt{RT_{rm}}} (\frac{p_{atm}}{p_{rm}})^{\frac{1}{\gamma}} [\frac{2\gamma}{\gamma - 1} [1 - (\frac{p_{atm}}{p_{rm}})^{\frac{\gamma-1}{\gamma}}]]^{\frac{1}{2}} \tag{2.85}$$

and critical flow is given by

$$\dot{m}_{rm,o} = \frac{C_{D,rm} A_{T,rm} p_{rm}}{\sqrt{RT_{rm}}} \gamma^{\frac{1}{2}} (\frac{2}{\gamma + 1})^{\frac{\gamma+1}{2(\gamma-1)}} \tag{2.86}$$

where $C_{D,rm}$ and $A_{T,rm}$ are constants. $A_{T,rm}$ can be a variable for regulating return manifold pressure, effecting cathode pressure.

The air entering the stack must be cooled as it leaves the compressor. Heat transfer effects are not studied in the model and an ideal cooler is assumed that maintains the temperature at $80^{\circ}$ C. However, temperate change does effect humidity of the gas. The pressure drop across the air cooler is considered negligible. The air cooler humidity ($\phi_{cl}$) is calculated as follows:

$$\phi_{cl} = \frac{p_{v,cl}}{p_{sat} T_{cl}} = \frac{p_{cl} p_{v,atm}}{p_{atm} p_{sat} T_{cl}} = \frac{p_{cl} \phi_{atm} p_{sat}}{p_{atm} p_{sat} T_{cl}} \tag{2.87}$$

The mass of the gas does not change with temperature, thus the air cooler mass flow rate is equivalent to the supply manifold outlet mass flow rate.

Water vapor is injected into the air flow exiting the air cooler, just before entering the fuel cell stack. The volume of the humidifier is small and thus treated as a part of the supply manifold volume. The air temperature is considered constant during this process. With a knowledge of the air flow exiting the humidifier, the dry mass air flow rate $\dot{m}_{air,cl}$, the vapor mass flow rate $\dot{m}_{v,cl}$, and the dry air pressure $p_{air,cl}$ can be determined through thermodynamic equations. The vapor saturation pressure $p_{v,cl}$ is determined by

$$p_{v,cl} = \phi_{cl} p_{sat} T_{cl} \tag{2.88}$$

and the difference between total pressure and vapor pressure will determine the dry air pressure $p_{air,cl}$ by

$$p_{air,cl} = p_{cl} - p_{v,cl} \tag{2.89}$$

leading to the humidity ratio ($\omega_{cl}$) with

$$\omega_{cl} = \frac{M_v p_{v,cl}}{M_{air} p_{air,cl}} \tag{2.90}$$

where $M_{air}$ is the molar mass of dry air and $M_v$ is the molar mass of vapor. Once the humidity ratio is determined the mass flow rate of dry air and vapor can be determined with the following

$$\dot{m}_{air,cl} = \frac{1}{1+\omega_{cl}} \dot{m}_{cl} \tag{2.91}$$

$$\dot{m}_{v,cl} = \dot{m}_{cl} - \dot{m}_{air,cl} \tag{2.92}$$

The mass flow rate of air does not change in the humidifier, but the additional water vapor increases the mass flow rate of vapor

$$\dot{m}_{v,hm} = \dot{m}_{v,cl} + \dot{m}_{v,inj} \tag{2.93}$$

where $\dot{m}_{v,inj}$ is injected water vapor. Increasing the vapor mass also increases the vapor pressure ($p_{v,hm}$) which is determined by

$$p_{v,hm} = \frac{\dot{m}_{v,hm} M_{air}}{\dot{m}_{air,cl} M_v} p_{air,cl} \tag{2.94}$$

allowing for the calculation of the humidifier exit humidity ($\phi_{hm}$)

$$\phi_{hm} = \frac{p_{v,hm}}{p_{sat} T_{hm}} = \frac{p_{v,hm}}{p_{sat} T_{cl}} \tag{2.95}$$

The total pressure in the humidifier increases because the vapor pressure increases, thus

$$p_{hm} = p_{air,cl} + p_{v,hm} \tag{2.96}$$

where $p_{air,cl}$ is the cooler dry air pressure and $p_{v,hm}$ is the humidifier vapor pressure. The humidifier exit flow mass continuity is given by

$$\dot{m}_{hm} = \dot{m}_{air,cl} + \dot{m}_{v,cl} + \dot{m}_{v,inj} \tag{2.97}$$

where $\dot{m}_{air,cl}$ and $\dot{m}_{v,cl}$ are the air and vapor entering the humidifier and $\dot{m}_{v,inj}$ is the added

water vapor. The exit flow from the humidifier is the cathode inlet flow.

## 2.3 Model Deficiencies

The automotive fuel cell model by Pukrushpan *et al.* [3] is excellent for studying reactant gas control strategies but lacks the capability for a more detailed analysis, particularly a single cell failure. Long transients such as thermal changes and inert gas build-up are also ignored. The small time transient of the charge double layer is also neglected. Each of these can temporarily effect a fuel cell voltage reading. Thus, a direct reading of fuel cell voltage at a given current does not give enough information to describe the system health. Each deficiency addressed in this thesis is discussed in this section.

#### Cell Variation

This model simulates a single fuel cell and generates a stack by multiplying the one cell by $N_{fc}$. A real system has variations between cells due to manufacturing and design. Other variations may occur due to non-uniform stack temperature, non-uniform distribution of reactants, or degradation. Without a separation of cell model, a parameter change will effect the entire stack, thus affecting the system controls more significantly than a single cell with modified parameters.

#### Thermal Subsystem

A thermal system will impact the response of the fuel cell stack. Operational temperature has a direct effect on operational voltage. Parasitic losses are also effected as pumps and valves are actuated. Vasu *et al.* [33] explored a thermal model for an automotive fuel cell stack. Results show different voltage patterns when the thermal system is accounted. The stack settling time is approximately 50 min in an open-loop scenario and with tuning, approximately 6 min in a closed-loop scenario.

**Inert Gas Build-up**

Inert gasses can limit fuel cell performance. These gases, particularly nitrogen, can build up on the anode side of the fuel cell. Nitrogen enters through both non-pure hydrogen fuel cells and by permeation through the MEA [34]. Fuel cells do not operate at 100% fuel utilization per pass, and thus spent anode gas is recycled to the anode inlet. This recirculation compounds the inert gas build up. Nitrogen can be controlled by periodic or continuous purging. The purge should be minimized because the hydrogen is lost irrecoverably. It may also have to be treated to avoid a safety hazard. Nitrogen build up decreases the hydrogen partial pressure, reducing hydrogen fuel utilization.

**Charge Double Layer**

The charge double layer phenomena is not incorporated into the Pukrushpan fuel cell model. There is debate about the importance of the effect of the charge double layer [35]. Pukrushpan decided to neglect the charge double layer because the time constant is significantly smaller than reactant gas transients. However, the time constant referenced is for a single cell and not a stack. Introducing the charge double layer effect also allows for an effective technique to determine a cell's ohmic resistance.

**Liquid Water**

Liquid water is ignored in the automotive fuel cell model. Liquid water can cause abnormal pressure drops, starvation of the MEA, and irregular voltage patterns. Liquid water is more prevalent on the cathode than the anode due to the production of $H_2O$ on the cathode. It is possible for the cathode channels to be flooded while the anode channels are dry, creating an environment of difficult water management. Liquid water transients are shown to be on a time scale of twenty minutes [13]. The model as designed often contains a quantity of liquid water throughout operation, and the membrane humidification is kept at a constant 100% humidity.

**Humidity Control**

Humidity control is neglected and perfect humidification is assumed, despite containing a humidification model. Humidity is often controlled by manipulating stack temperature. This is not possible without a thermal model. Modifying stack temperature to maintain a healthy membrane will effect the voltage and thus should be included.

# Chapter 3

# Model Enhancements

Additional features are added to Pukrushpan's fuel cell model to implement classification techniques on a more complex system. Pukrushpan *et al.* [3] did not include various features since they were outside of his scope. These features are necessary to more realistically model an automotive proton exchange membrane fuel cell. Transient information may be useful in fault classification. It may also cause difficulties in fault classification by creating outliers in the data. These are challenges in classification that must be addressed.

The most critical addition is the development of a multi-cell model. It is necessary to understand how a single dysfunctional cell can impact the dynamics of an entire stack, if at all. In addition to the multi-cell model a thermal system is highly critical. A fuel cell stack experiences temperature swings as power demands change. The system will attempt to maintain a consistent stack temperature but it provides an easy means to modifying the relative humidity of the stack. This is of extreme importance to maintaining membrane health. Inert gas build-up is also a significant issue for automotive PEMFCs. Maintaining a high hydrogen fuel efficiency requires a dead-end mode or recycling of the fuel. In both these scenarios nitrogen builds up either through impure fuel sources or through nitrogen crossover. This is mitigated when a system vents directly to atmosphere.

Each of these effects are a part of normal operation and will decrease a fuel cell's voltage. An efficient and effective classifier must be capable of discriminating between normal operation (recoverable voltage losses) and deteriorated operation (non-recoverable voltage loss).

## 3.1 Multi-Cell Development

The fuel cell system model is enhanced by supplementing the fuel cell stack assembly with an additional single cell model. This enables the analysis of a single cell in various failure modes in a fuel cell system. The fuel cell cathode and anode volumes corresponded to a 381 cell system. As such the fuel cell volumes were reduced respectively. The stack was reduced to 380 cells and a single cell was added in parallel. The cathode and anode mass flow rates are split with a ratio of 380/381 of the flow entering the stack, and 1/381 entering the single cell. The fuel cell temperature and relative humidities entering the stack and cell are not modified. Upon leaving the stack and cell, the mass flow rates are added to each other. The temperatures and relative humidities exiting are proportionately combined. It is possible to test the effect of reduced temperature and/or relative humidity on a single cell. Figure 3.1 demonstrates the separation of inlet flows and the combination of outlet flows.

The various failure modes are generated with gains in the single cell model only. These gains modify the ohmic loss, the concentration loss, and activation loss in the stack voltage model. The nitrogen permeation model includes a gain to modify nitrogen permeation rate. Another set of gains modify the flow of hydrogen to both the stack and the single cell. In the event of a blockage, excess hydrogen may enter the fuel cell stack rather than the single fuel cell.

The stack voltage model and individual cell model are compared to validate the results of the single cell. Small variations in data occur on a scale of $10^{-7}$ or less. This variation

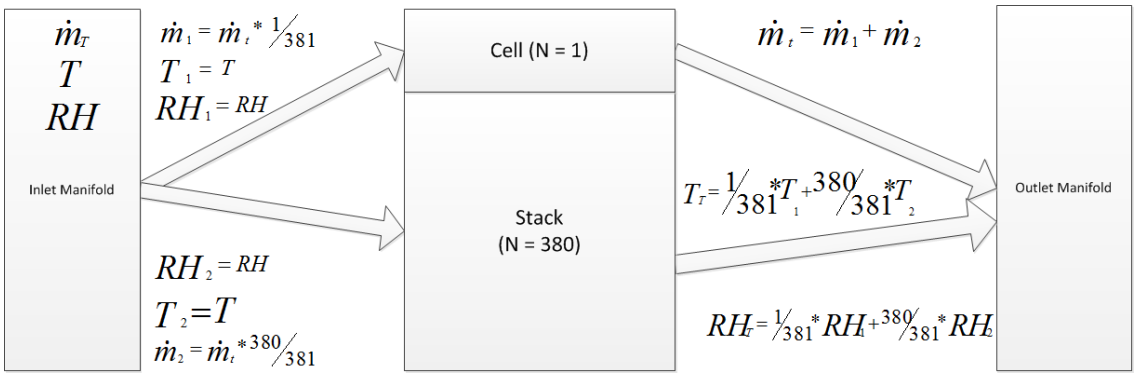


Figure 3.1: Diagram of Stack and Cell Flow Separation

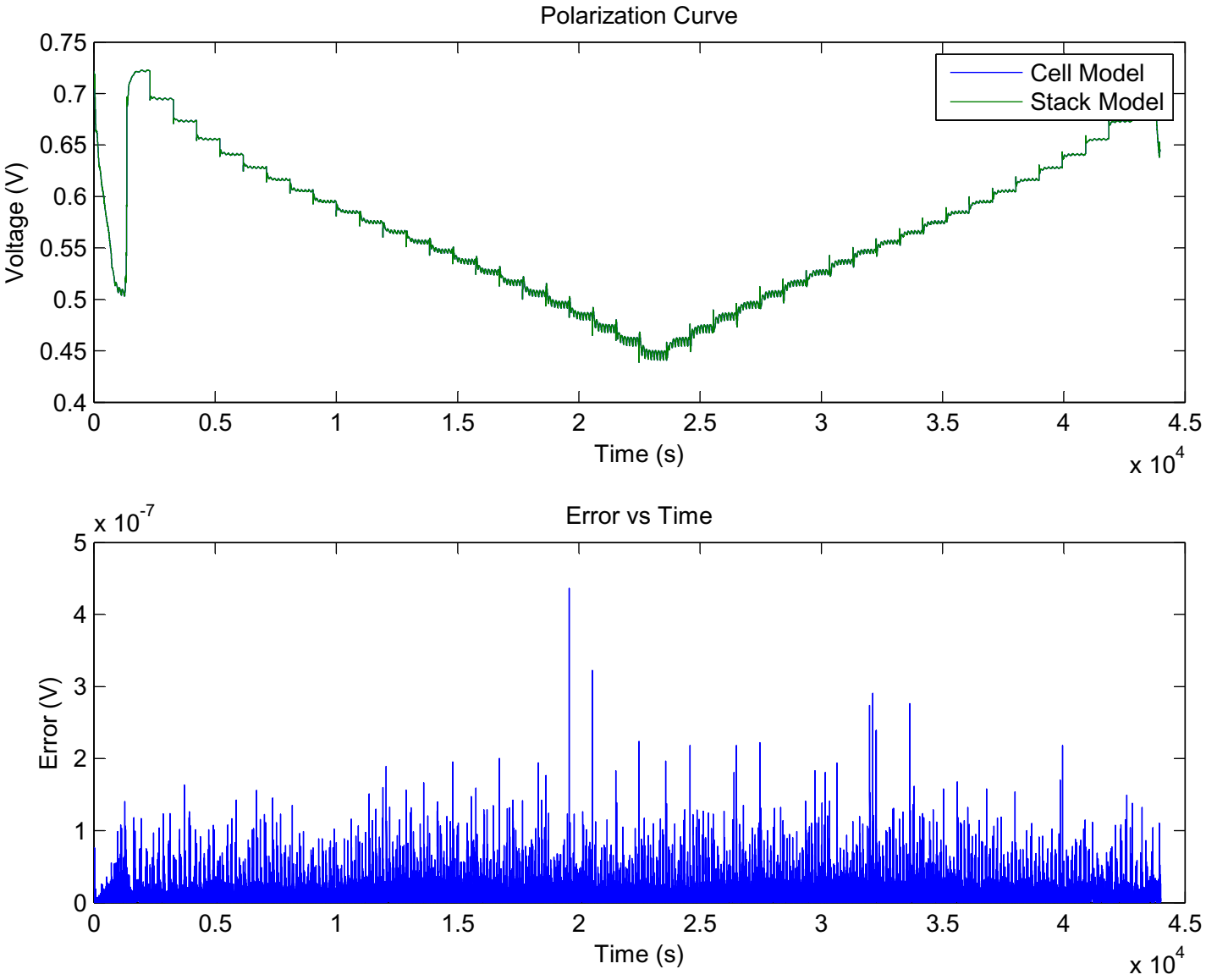


Figure 3.2: Comparison of Stack and Cell Model Results

is due to the limited nature of a numerical analysis. A plot of error versus time can be seen in Figure 3.2.

## 3.2 Double Charge Layer

The effect of the double charge layer is included in the enhanced automotive fuel cell model. The capacitive effect is modeled by

$$C\frac{dV_{dyn}}{dt} = A_{membr}i(1 - \frac{V_{dyn}}{V_{act} + V_{conc}}) \tag{3.1}$$

The overall voltage equation must be restated with the dynamic voltage loss term

$$V = E - V_{dyn} - V_{ohm} \tag{3.2}$$

Pukrushpan states that the charge double layer effect is negligible due to its small time constant. Meyer *et al.* [35] determined the effect is only important when interested in time scales smaller than the 2% settling time. The 2% settling time varies with the capacitance of the system, in Meyer *et al.* this is a few tenths of a second. A fuel cell typically has a capacitance in the range of a few farads [1]. For the purposes of this research a 3 farad capacitance is selected.

The double charge layer effect is included to expand the functionality of the model. The current stop test shown in Figure 1.8 explains how this effect could be used to determine the ohmic loss at a specific current density. This information could represent an additional feature for pattern recognition in health classification.

## 3.3 Nitrogen Permeation

Nitrogen has two methods of entering the anode. Nitrogen may enter through as a part of the fuel supply since pure hydrogen is difficult to obtain. In this model the $H_2$ storage tanks are assumed to be 99.925% pure. The second method of transport is permeation across the MEA. According to Ahluwalia *et al.* [34] the permeation of nitrogen per unit area $dN_{N_2}/dA$ can be expressed in the form

$$\frac{dN_{\mathrm{N}_2}}{dA} = \frac{\psi_{\mathrm{N}_2}}{\delta_m}(P^c_{\mathrm{N}_2} - P^a_{\mathrm{N}_2}) \tag{3.3}$$

Where $\psi_{\mathrm{N}_2}$ is the permeance in mol/(cm*s*bar)

$\delta_m$ is the thickness of the membrane in cm

$P^c_{\mathrm{N}_2}$ is the nitrogen pressure at the cathode in bar

$P^a_{\mathrm{N}_2}$ is the nitrogen pressure at the anode in bar

$$\psi_{\mathrm{N}_2} = (0.0295 + 1.21 f_v - 19.3 f_v^2) \times 10^{-11} \times \exp[\frac{E_{\mathrm{N}_2}}{R_{N_2}}(\frac{1}{T_{ref}} - \frac{1}{T_{fc}})] \tag{3.4}$$

where $f_v$ is the volume fraction of water

$E_{\mathrm{N}_2}$ is 24 kJ/mol

$R_{N_2}$ is the nitrogen gas constant kJ/(kg K)

$T_{ref}$ is $303K$

The volume fraction of water is determined by manipulating the term $\lambda_m$, a ratio of $H_2O$ to $SO_3^-$. The automotive fuel cell model incorporates $\lambda_m$ as a component of the membrane humidification model. The volume fraction of water is defined from percolation theory:

$$f_v = \frac{V_{water}}{V_{water} + (V_d - V_p)} \tag{3.5}$$

where $V_{water}$ is the volume fraction of water

$V_d$ is volume of the dry membrane

$V_p$ is volume of the membrane that does not interact with water

The volume $V_p$ is considered negligible. $V_d$ is taken from the thickness of the membrane ($0.007$ in) and the cross sectional area (280 $cm^2$). The volume of water is a little more difficult to calculate.

Given that Nafion 117 is $C_7HF_{13}O_5SC_2F_4$ and the activity site is the $SO_3^-$ portion, a molar mass ratio can be determined.

$$\text{molar mass ratio} = \frac{\mathrm{SO}_3^-}{\mathrm{C}_7\mathrm{HF}_{13}\mathrm{O}_5\mathrm{SC}_2\mathrm{F}_4} = \frac{80.0632}{544.139} = 0.147137 \tag{3.6}$$

where Carbon is 12.0107 g/mol

Hydrogen is 1.00794 g/mol

Flourine is 18.9984032 g/mol

Oxygen is 15.9994 g/mol

Sulfur is 32.065 g/mol

This is compared to the mass ratio to determine the mass of the activity sites.

$$\text{molar mass ratio} = \frac{\text{moles of } SO_3^-}{\text{moles of } C_7HF_{13}O_5SC_2F_4} \tag{3.7}$$

With the known volume and density of nafion 117, the moles of $C_7HF_{13}O_5SC_2F_4$ are determined. With an active area of $280$ cm$^2$, a thickness of $0.0178$ cm, and a density of $2$ g/cm$^3$, the mass of the sulphates is $1.466661616$ grams.

$$\text{moles of } H_2O = \lambda_m \times 0.018318798 \text{ moles of } SO_3^- \tag{3.8}$$

Equation 3.8 is used to determine the number of moles of $H_2O$ in the membrane. This leads to the water mass. A water volume is calculated at 80 degrees Celsius in one atmosphere of pressure. The volume fraction of water is determined using Equation 3.5, and used to calculate the permeance in Equation 3.4, which is used to calculate the permeation of nitrogen through the fuel cell in Equation 3.3.

The nitrogen model is included in the enhanced fuel cell model due to its effect on voltage. It represents one more degree of difficulty for the classifier. Figure 3.3 presents the gas flow rates going into and out of the anode volume, and nitrogen permeation across the MEA. The permeation rate increases as the polarization curve test draws more current. This is due in part to the increased anode and cathode pressures. The anode flow rates and nitrogen permeation plots are separated due to their different scales.

## 3.4 Anode Purge

An anode purge model is incorporated in the model to allow the release of nitrogen. This model reproduces the cathode outlet manifold model and incorporates it as the anode outlet

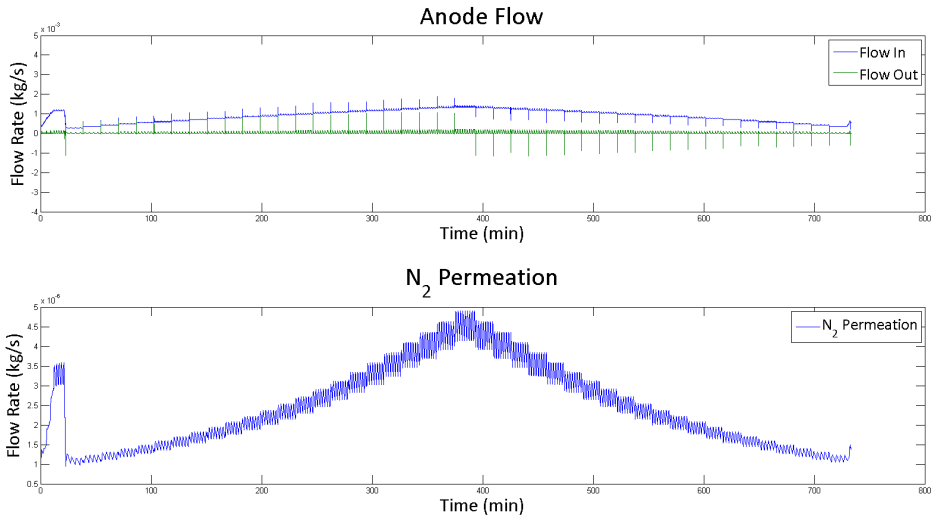


Figure 3.3: Nitrogen Permeation Rate during a Polarization Curve Test

manifold model. The area of the outlet manifold nozzle is used to control the flow rate of the hydrogen. An anode purge control system manipulates the flow to obtain different humidities, pressures, and to operate in anode cleansing operations.

The anode outlet manifold has a small temperature drop and a large pressure drop, thus modeled by

$$\frac{dp_{rm,a}}{dt} = \frac{R_{rm,a}T_{rm,a}}{V_{rm,a}}(\dot{m}_{a,o} - \dot{m}_{rm,a,o}) \tag{3.9}$$

where $V_{rm,a}$ is the volume of the anode return manifold and $T_{rm,a}$ is the temperature of the anode return manifold gasses. $R_{rm,a}$ is a composition of the nitrogen gas constant ($R_{N_2}$), the water vapor gas constant ($R_v$), and the hydrogen gas constant ($R_{H_2}$). The nonlinear nozzle equation for subcritical flow is given by

$$\dot{m}_{rm,a,o} = \frac{C_{D,rm,a}A_{T,rm,a}p_{rm,a}}{\sqrt{\bar{R}T_{rm,a}}}(\frac{p_{atm}}{p_{rm,a}})^{\frac{1}{\gamma}}[\frac{2\gamma}{\gamma-1}[1-(\frac{p_{atm}}{p_{rm,a}})^{\frac{\gamma-1}{\gamma}}]]^{\frac{1}{2}} \tag{3.10}$$

and critical flow is given by

$$\dot{m}_{rm,a,o} = \frac{C_{D,rm,a}A_{T,rm,a}p_{rm,a}}{\sqrt{\bar{R}T_{rm,a}}}\gamma^{\frac{1}{2}}(\frac{2}{\gamma+1})^{\frac{\gamma+1}{2(\gamma-1)}} \tag{3.11}$$

where $C_{D,rm,a}$ is a constant and $A_{T,rm,a}$ is the controllable value for purging. $\gamma$ is a ratio

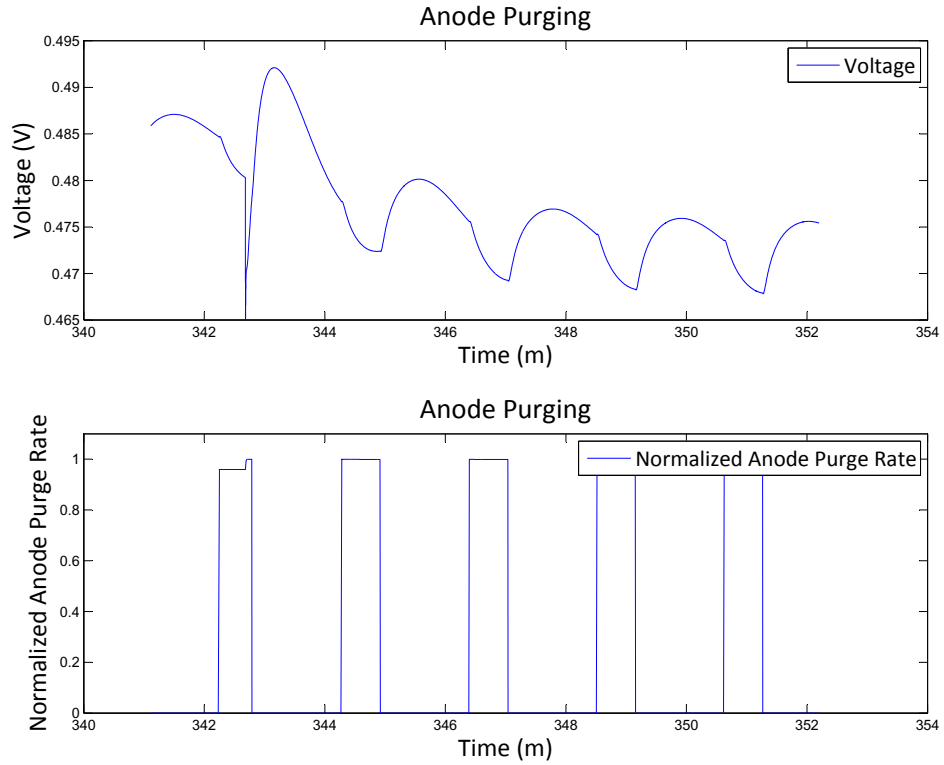


Figure 3.4: Voltage Effects during Anode Purging

for specific heat.

Control methods are not the intent of the study; as such a simple threshold based purging design is employed. Each time the nitrogen content crosses a high threshold, the valve opens until the nitrogen content has been reduced to a low threshold. These values create different voltage characteristics when adjusted. If a relatively low nitrogen content is used as the high threshold, purging operations will occur often and rapidly. A high nitrogen content as a threshold leads to large voltage swings unless the purge rate is kept low. Some of these characteristics could be controlled or modified by leading the purge with increased hydrogen pressure. For this work the relay attempts to hold the hydrogen mole fraction between 85% and 97%.

The effect of a purge at steady state can be seen in Figure 3.4. In this figure current

draw is stepped up near the beginning of the time frame. The system then reaches steady state where it cycles between high and low voltages. The lowest voltages are reached at the end of the purge. During a purge operation hydrogen pressure is decreased creating a temporary activation loss. Humidity is also expelled from the system increasing ohmic resistance. After the purge operation ceases voltages climb rapidly as hydrogen pressure returns and humidity returns to normal. However, nitrogen content also increases steadily through this transient eventually creating larger losses, and the system is purged again.

## 3.5 Humidification Controls

Fuel cell membrane humidification is important to a fuel cell system but it is difficult to measure and control. Relative humidity is measured at the outlet of the cathode and this feeds a PI controller in the thermal system. Manipulating the thermal temperature of a fuel cell stack can rapidly change the water content within the system. The fuel cell stack temperature controller attempts to maintain a stack temperature of 353 degrees Kelvin. This temperature is modified as needed by the humidifier controller to achieve a desired relative humidity.

Humidity sensors cannot react instantaneously to changes. Depending on the type, temperature range, and humidity range their response times can vary from seconds to minutes [36]. As such, a time lag is applied to the model's calculated humidity by the transfer function below. Equation 3.12 approximates a 30 second time constant.

$$TF = \frac{1}{30s + 1} \tag{3.12}$$

## 3.6 Thermal Model

The enhanced automotive fuel cell model incorporates a thermal subsystem to model transient behavior. Fuel cell voltage is effected by stack temperature. The Pukrushpan model does not incorporate these dynamics as their time constant is outside of his scope. By incorporating a thermal model a method for humidification control becomes available. This

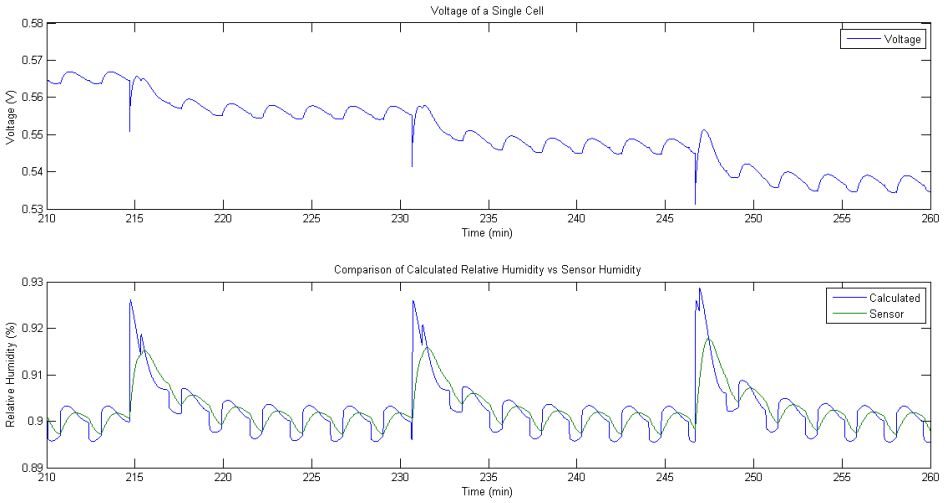


Figure 3.5: Relative Humidity Sensor Results for Humidity Control

is important as it introduces new transients to the system.

The energy in each control volume (cathode, anode, stack) is modeled by the conservation of energy. Enthalpy is used to replace the sum of thermal energy and flow work per unit mass. The kinetic and potential energy effects of the gas are assumed negligible. This simplifies the equation to

$$\frac{dE_s}{dt} = \dot{m}(i)_{in} - \dot{m}(i)_{out} + q \tag{3.13}$$

where $\dot{m}$ is the mass flow rate in kg/s and $q$ is heat transfer in watts.

### 3.6.1 Stack and Channels

Employing conservation of energy on the anode channel leads to

$$\begin{aligned}\frac{dE_a}{dt} &= \dot{m}_{\mathrm{H}_2,i}h_{\mathrm{H}_2,i} + \dot{m}_{\mathrm{N}_2,i}h_{\mathrm{N}_2,i} + \dot{m}_{\mathrm{H}_2\mathrm{O},i}h_{\mathrm{H}_2\mathrm{O},i} \\ &\quad - \dot{m}_{\mathrm{H}_2,o}h_{\mathrm{H}_2,o} - \dot{m}_{\mathrm{N}_2,o}h_{\mathrm{N}_2,o} - \dot{m}_{\mathrm{H}_2\mathrm{O},o}h_{\mathrm{H}_2\mathrm{O},o} \\ &\quad - \dot{m}_{\mathrm{H}_2,rx}h_{\mathrm{H}_2,rx} + \dot{m}_{\mathrm{N}_2,diff}h_{\mathrm{N}_2,diff} - \dot{m}_{\mathrm{H}_2\mathrm{O},diff}h_{\mathrm{H}_2\mathrm{O},diff}\end{aligned} \tag{3.14}$$

Where $\dot{m}_{\mathrm{H}_2,i}$ is the mass flow rate in of hydrogen entering the anode
$h_{\mathrm{H}_2,i}$ is the specific enthalpy of hydrogen entering the anode
$\dot{m}_{\mathrm{N}_2,i}$ is mass flow rate of nitrogen entering the anode
$h_{\mathrm{N}_2,i}$ is the specific enthalpy of nitrogen entering the anode
$\dot{m}_{\mathrm{H}_2\mathrm{O},i}$ is the mass flow rate of water entering the anode
$h_{\mathrm{H}_2\mathrm{O},i}$ is the specific enthalpy of water entering the anode
$\dot{m}_{\mathrm{H}_2,o}$ is the mass flow rate in of hydrogen exiting the anode
$h_{\mathrm{H}_2,o}$ is the specific enthalpy of hydrogen exiting the anode
$\dot{m}_{\mathrm{N}_2,o}$ is mass flow rate of nitrogen exiting the anode
$h_{\mathrm{N}_2,o}$ is the specific enthalpy of nitrogen exiting the anode
$\dot{m}_{\mathrm{H}_2\mathrm{O},o}$ is the mass flow rate of water exiting the anode
$h_{\mathrm{H}_2\mathrm{O},o}$ is the specific enthalpy of water exiting the anode
$\dot{m}_{\mathrm{H}_2,rx}$ is the mass flow rate of hydrogen reacting across the membrane
$h_{\mathrm{H}_2,rx}$ is the specific enthalpy of hydrogen reacting across the membrane
$\dot{m}_{\mathrm{N}_2,diff}$ is mass flow rate of nitrogen diffusing across the membrane
$h_{\mathrm{N}_2,diff}$ is the specific enthalpy of nitrogen diffusing across the membrane
$\dot{m}_{\mathrm{H}_2\mathrm{O},diff}$ is the mass flow rate of water diffusing across the membrane
$h_{\mathrm{H}_2\mathrm{O},diff}$ is the specific enthalpy of water diffusing across the membrane

The cathode control volume utilizes a similar analysis that leads to

$$\begin{aligned}\frac{dE_c}{dt} &= \dot{m}_{\mathrm{O}_2,i}h_{\mathrm{O}_2,i} + \dot{m}_{\mathrm{N}_2,i}h_{\mathrm{N}_2,i} + \dot{m}_{\mathrm{H}_2\mathrm{O},i}h_{\mathrm{H}_2\mathrm{O},i} \\ &\quad - \dot{m}_{\mathrm{O}_2,o}h_{\mathrm{O}_2,o} - \dot{m}_{\mathrm{N}_2,o}h_{\mathrm{N}_2,o} - \dot{m}_{\mathrm{H}_2\mathrm{O},o}h_{\mathrm{H}_2\mathrm{O},o} \\ &\quad - \dot{m}_{\mathrm{O}_2,rx}h_{\mathrm{O}_2,rx} - \dot{m}_{\mathrm{N}_2,diff}h_{\mathrm{N}_2,diff} \\ &\quad + \dot{m}_{\mathrm{H}_2\mathrm{O},diff}h_{\mathrm{H}_2\mathrm{O},diff} + \dot{m}_{\mathrm{H}_2\mathrm{O},gen}h_{\mathrm{H}_2\mathrm{O},gen}\end{aligned} \tag{3.15}$$

The temperature in both the anode and cathode are determined by dividing the energy term by the thermal mass of each system.

The fuel cell body consists of multiple volumes and masses such as the cooling channels, anode volume, cathode volume, bipolar plates, cooling plates, membranes, etc. It is

assumed the mass transfer into and out of the diffusion layers are neglible and that conservation of energy is more practical than conservation of mass on the fuel cell body. Conservation of energy in the fuel cell body leads to

$$\begin{aligned} m_{fc}c_{v,fc}\frac{dT_{fc}}{dt} &= \dot{m}_{\mathrm{H}_2,rx}C_{p,\mathrm{H}_2}(T_a - T_{fc}) + \dot{m}_{\mathrm{H}_2,co}h_{\mathrm{H}_2}(T_a) + \\ &\quad \dot{m}_{\mathrm{O}_2,rx}C_{p,\mathrm{O}_2}(T_c - T_{fc}) + \dot{m}_{\mathrm{O}_2,co}h_{\mathrm{O}_2}(T_c) \\ &\quad - \dot{m}_{\mathrm{H_2O},membr\to a}h_{f,\mathrm{H_2O}}(T_{fc}) - \dot{m}_{\mathrm{H_2O},membr\to c}h_{f,\mathrm{H_2O}}(T_{fc}) \\ &\quad - h_{c,a}A_a(T_{fc} - T_a) - h_{c,c}A_c(T_{fc} - T_c) \\ &\quad - h_{c,amb}A_{fc}(T_{fc} - T_{amb}) - h_{c,clt,fc}A_{clt,fc}(T_{fc} - T_{clt,fc}) \\ &\quad + N_{fc}A_{membr}i(E_{th} - V) \end{aligned} \tag{3.16}$$

Where $m_{fc}$ is the mass of the fuel cell

$c_{v,fc}$ is the average specific heat at constant volume of the fuel cell

$\dot{m}_{\mathrm{H}_2,rx}$ is mass flow of hydrogen reacting

$C_{p,\mathrm{H}_2}$ is average specific heat of hydrogen

$T_a$ is temperature of the anode

$T_{fc}$ is the temperature of the cathode

$\dot{m}_{\mathrm{H}_2,co}$ is the mass flow rate of hydrogen crossover

$h_{\mathrm{H}_2}$ is the specific enthalpy of hydrogen

$\dot{m}_{\mathrm{O}_2,rx}$ is mass flow rate of oxygen reacting

$C_{p,\mathrm{O}_2}$ is average specific heat of oxygen

$T_c$ is the temperature of the cathode

$\dot{m}_{\mathrm{O}_2,co}$ is the mass flow rate of oxygen crossover

$h_{\mathrm{O}_2,o}$ is the specific enthalpy of oxygen

$\dot{m}_{\mathrm{H_2O},membr\to a}$ is mass flow of water from the membrane to the anode

$h_{l,\mathrm{H_2O}}$ is specific enthalpy of liquid water

$\dot{m}_{\mathrm{H_2O},membr\to c}$ is mass flow of water from the membrane to the cathode

$h_{c,a}$ is convective heat transfer coefficient in the anode

$A_a$ is area of the anode

$h_{c,c}$ is convective heat transfer coefficient in the cathode

$A_c$ is the area of the cathode

$h_{c,amb}$ is convective heat transfer coefficient to ambient air

$A_{fc}$ is area of the fuel cell in ambient air

$h_{c,clt,fc}$ is convective heat transfer coefficient of the fuel cell coolant

$A_{clt,fc}$ is area the coolant contacts the fuel cell

$T_{clt,fc}$ is temperature of the fuel cell coolant

$N_{fc}$ is the number of cells

$A_{membr}$ is the area of the membrane

$i$ is current

$E_{th}$ is reversible voltage

$V$ is fuel cell voltage

However, for the purposes of this research the anode and cathode control volumes can be assumed equivalent to the stack temperature. The difference is considered negligible. This negates the concern for convection within the anode and cathode channels. Further research could investigate the effects of convection, which would likely have the greatest effect at high flow rates. Oxygen crossover and hydrogen crossover are neglected as well. The focus is the coolant flow and heat generated. This reduces the previous equation to the following

$$m_{fc}c_{v,fc}\frac{dT_{fc}}{dt} = -h_{c,clt,fc}A_{clt,fc}(T_{fc} - T_{clt,fc}) + N_{fc}I(E_{th} - V) \tag{3.17}$$

### 3.6.2 Coolant Loop

The coolant loop seen in Figure 3.6 is modeled by the equations below. Four control volumes are used to model the coolant loop. These are the cooling channels within the fuel cell, the cooling channels within the heat exchanger, the air volume around the heat exchanger, and the heat exchanger body.

$$m_{clt,fc}c_{v,clt}\frac{dT_{clt,fc}}{dt} = \dot{m}_{clt}h_{clt}(T_{clt,fc,i} - T_{clt,fc}) + h_{c,clt,fc}A_{clt,fc}(T_{fc} - T_{clt,fc}) \quad (3.18)$$

$$m_{clt,hex}c_{v,clt}\frac{dT_{clt,hex}}{dt} = \dot{m}_{clt}h_{clt}T_{clt,fc} - \dot{m}_{clt}h_{clt}T_{clt,hex} + h_{c,clt,hex}A_{clt,hex}(T_{clt,hex} - T_{hex}) \quad (3.19)$$

$$m_{ha,hex}c_{v,ha,hex}\frac{dT_{ha,hex}}{dt} = \dot{m}_{ha,hex}h_{ha}T_{ha,i} - \dot{m}_{ha,hex}h_{ha}T_{ha,hex} + h_{c,ha,hex}A_{ha,hex}(T_{hex} - T_{ha,hex}) \quad (3.20)$$

$$m_{hex}c_{v,hex}\frac{dT_{hex}}{dt} = h_{c,clt,hex}A_{clt,hex}(T_{clt,hex} - T_{hex}) - h_{c,air,hex}A_{ha,hex}(T_{hex} - T_{ha,hex}) \quad (3.21)$$

The fuel cell coolant $T_{clt,fc}$ and heat exchanger coolant $T_{clt,hex}$ are mixed by a proportional valve control. This mixing changes the fuel cell inlet temperature $T_{clt,fc,i}$.

$$T_{clt,fc,i} = uT_{clt,hex} + (1 - u)T_{clt,fc} \quad (3.22)$$

where $u$ is the percent of mass flow through the heat exchanger.

A PI controller is used to manage the fuel cell coolant temperature at 353 degrees Kelvin. A pump runs at a continuous flow of $1.4$ kg/s through the coolant system. A controller modifies a valve position to separate flow between the heat exchanger and recirculating through the fuel cell body. The recirculation through the fuel cell body prevents hot spots during operation. Water is only sent through the heat exchanger when the coolant temperature is too high. A mass flow rate of air across the heat exchanger is assumed at 1.25 kg/s.

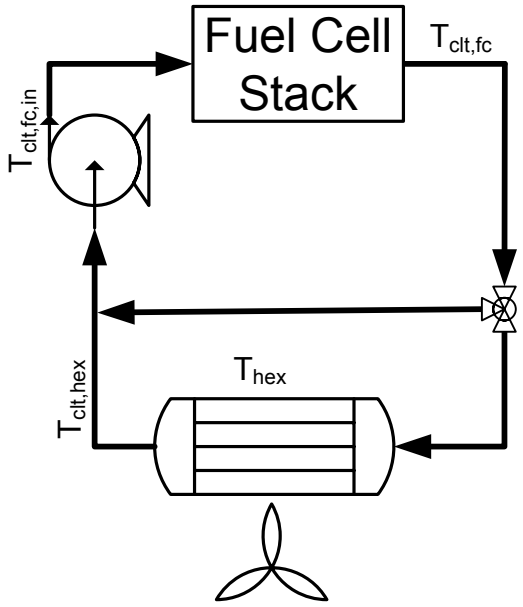


Figure 3.6: Coolant Loop

## 3.7 Membrane Hydration Correction

While working through Pukrushpan's model a strange phenomenon would occur at higher current densities. This phenomena caused a rapid voltage drop as membrane humidification crossed a certain threshold. The water diffiusion coefficient used in calculating electro-osmotic flow is non-continuous. Pukrushpan *et al.* used the following equations to determine determine molar flow rates of water through the membrane.

$$D_\omega = D_\lambda e^{2416(\frac{1}{303}-\frac{1}{T_{fc}})} \tag{3.23}$$

where $D_\omega$ is the water diffusion coefficient and $T_{fc}$ is the stack temperature.

$$D_\lambda = \begin{cases} 10^{-6} & \lambda_m < 2 \quad (3.24a) \\ 10^{-6}(1+2(\lambda_m-2)) & 2 \leq \lambda_m \leq 3 \quad (3.24b) \\ 10^{-6}(3-1.67(\lambda_m-3)) & 3 < \lambda_m < 4.5 \quad (3.24c) \\ 1.25*10^{-6} & \lambda_m \geq 4.5 \quad (3.24d) \end{cases}$$

where $\lambda_m$ is membrane water content.

Equation 3.24c is possibly incorrect with one coefficient and is rewritten as

$$D_\lambda = \begin{cases} 10^{-6}(3 - 1.167(\lambda_m - 3)) & 3 < \lambda_m < 4.5 \end{cases} \tag{3.25}$$

Figure 3.7 demonstrates the difference between the non-continuous and continuous equations. Pukrushpan *et al.* [4] discusses the use of his model at 100% humidification ($\lambda_m = 14$) due to "considerable drops in fuel cell voltage." The need to model the effects of varying membrane hydration led to this modification.

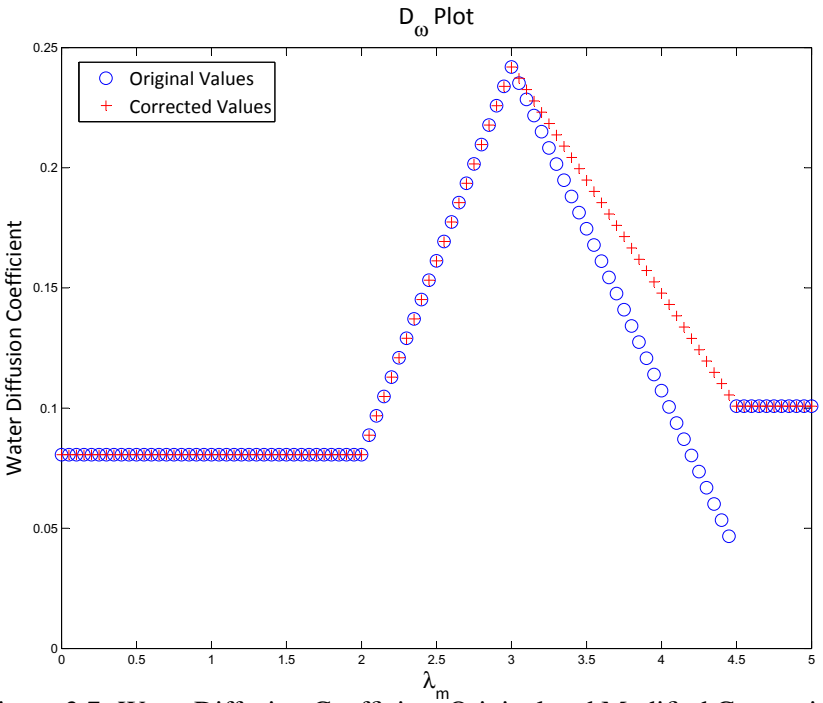


Figure 3.7: Water Diffusion Coefficient Original and Modified Comparison

## 3.8 Model Enhancement Results

The enhanced automotive fuel cell model successfully models the effects of the double charge layer, nitrogen permeation, anode purging, humidification controls, and thermal transients along with the capability to modify an individual cell. Figure 3.8 shows a step response of the average stack voltage and the step response of an individual cell with a 3% activation loss controlled at 87% humidification. The system experiences a drastic change

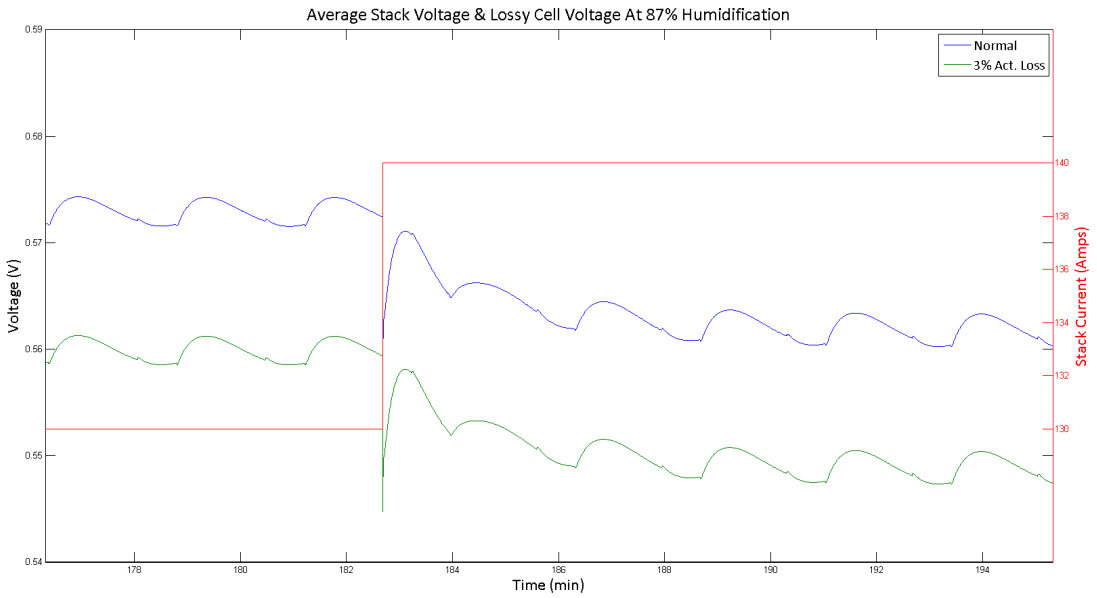


Figure 3.8: Average Stack Voltage and Lossy Cell Voltage Transients During a Current Step Increase and Anode Purging

as the stack current draw is increased. Hydrogen is let into the anode at an increased rate and cathode compressor spools up to maintain fuel cell operation. As the power draw increases the stack temperature and membrane water content increase, thus raising voltage. As the thermal system and membrane humidification respond the voltage reaches an oscillitory steady state. These oscillations are due to the periodic anode purging.

Figure 3.9 presents the temperature swings over the same time period as the step change in Figure 3.8. The stack fuel cell temperature is highest, followed by the fuel cell coolant outlet temperature. There is a large temperature difference between the fuel cell coolant and heat exchanger coolant. This is due to the bypass valve seen in Figure 3.6. Much of the fuel cell coolant loops back towards itself to maintain the correct temperature. The heat exchanger is the next highest temperature component, followed by the ambient temperature of air. Small variation in the temperatures can be seen as the system tries to maintain the cathode humidity near 87%. This is part of the response to the anode purging.

Figure 3.10 demonstrates the membrane water content response to both an increase in current draw and anode purging. During an increase in current draw the system generates

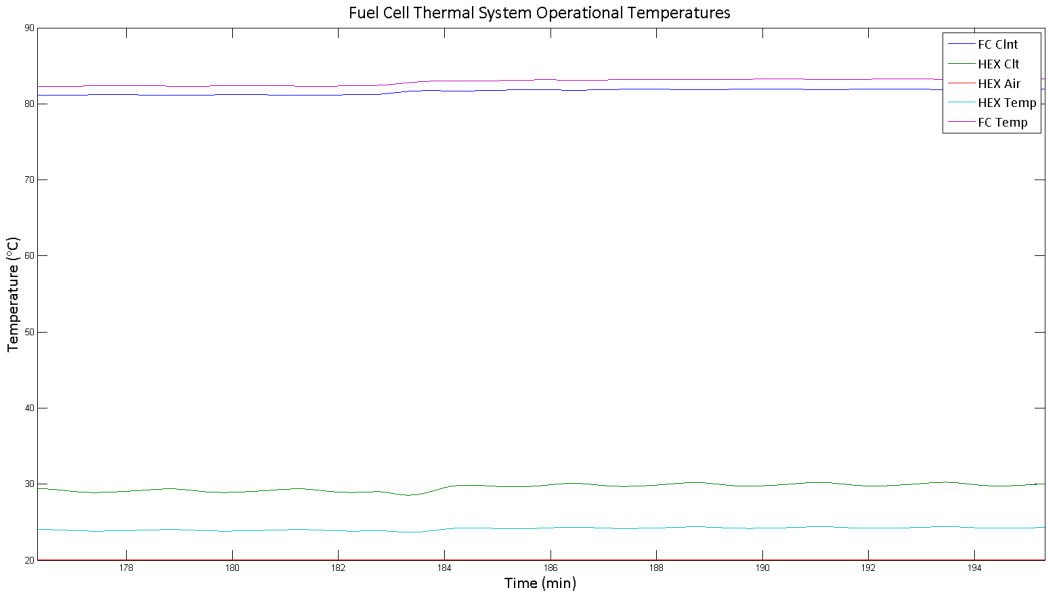


Figure 3.9: Thermal System Response to a Current Step Increase and Anode Purging

more water, increasing membrane humidification. It can be seen with each purge that membrane humidification significantly drops. The voltage loss during a purging operation is due to both the hydrogen pressure drop increasing the activation loss and the membrane humidification drop increasing the ohmic losses.

Figure 3.11 clearly shows the effect of a purging operation on the partial pressures within the anode volume. Vapor pressure is maintained at a fairly constant level throughout the fuel cell operation, while hydrogen pressure and nitrogen pressure significantly change. The nonlinear effect of the anode return manifold outlet nozzle is visible in the nitrogen partial pressure.

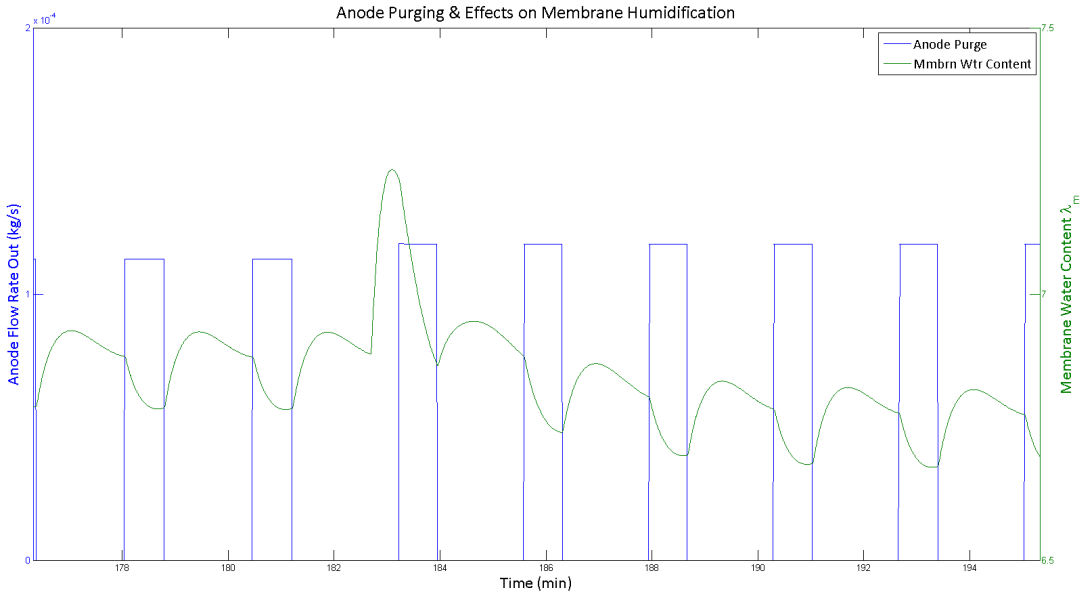


Figure 3.10: Membrane Water Content Response to Current Step Increase and Anode Purging

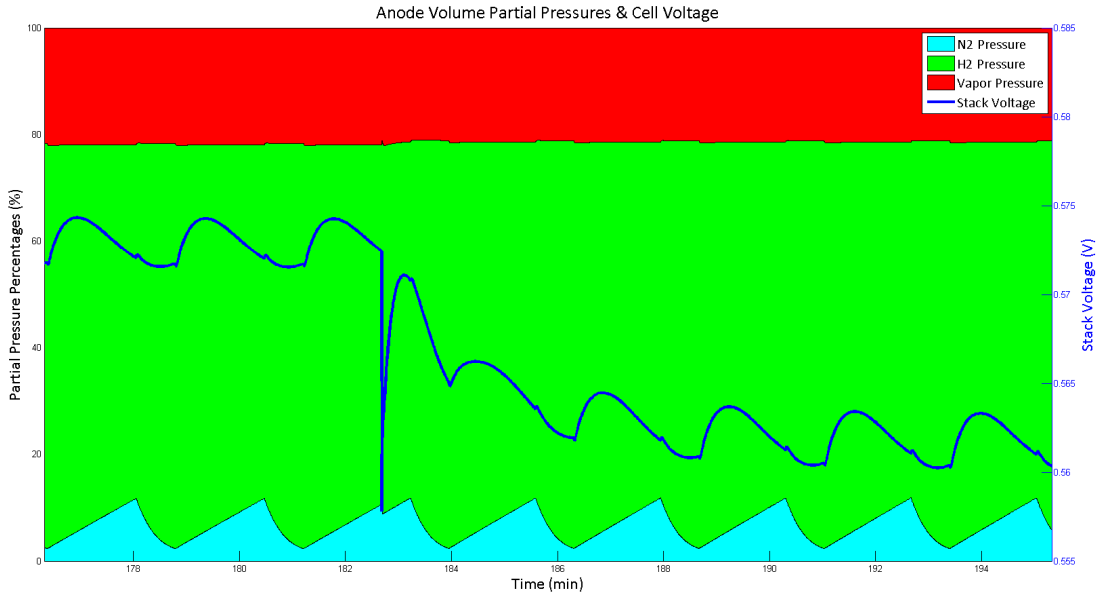


Figure 3.11: Anode Partial Pressure Response to a Current Step Increase and Anode Purging

# Chapter 4

# Prognostic Health Management

Prognostic health management (PHM) is a beneficial tool to optimize maintenance resources. It is used when condition based maintenance (CBM) is desired instead of a fixed schedule maintenance routine. PHM employs a variety of techniques to determine a system's or a component's state of health. These techniques include physics based models, artificial intelligence techniques, and probabilistic approaches [37]. Large complicated systems are difficult to model, in these circumstances a data based method is easier to implement.

Figure 4.1 shows the general concept behind a PHM system. Training data from known failure modes are the basis of the prognostic health management system. A component or system will produce outputs that are processed, features are selected, and if they fall within certain conditions a fault classification is determined. If a classification is not determined, the information is used for further training.

The development of a data-based prognostic health system requires training data to create the relationship between features and failure modes. These features are direct system outputs or transformations of the data via pre-processing techniques such as independent component analysis and principal component analysis. After training, a PHM system monitors system outputs and classifies the system state of health in real time. In adaptive systems, the classifications are used to adjust control strategies to improve remaining useful life.

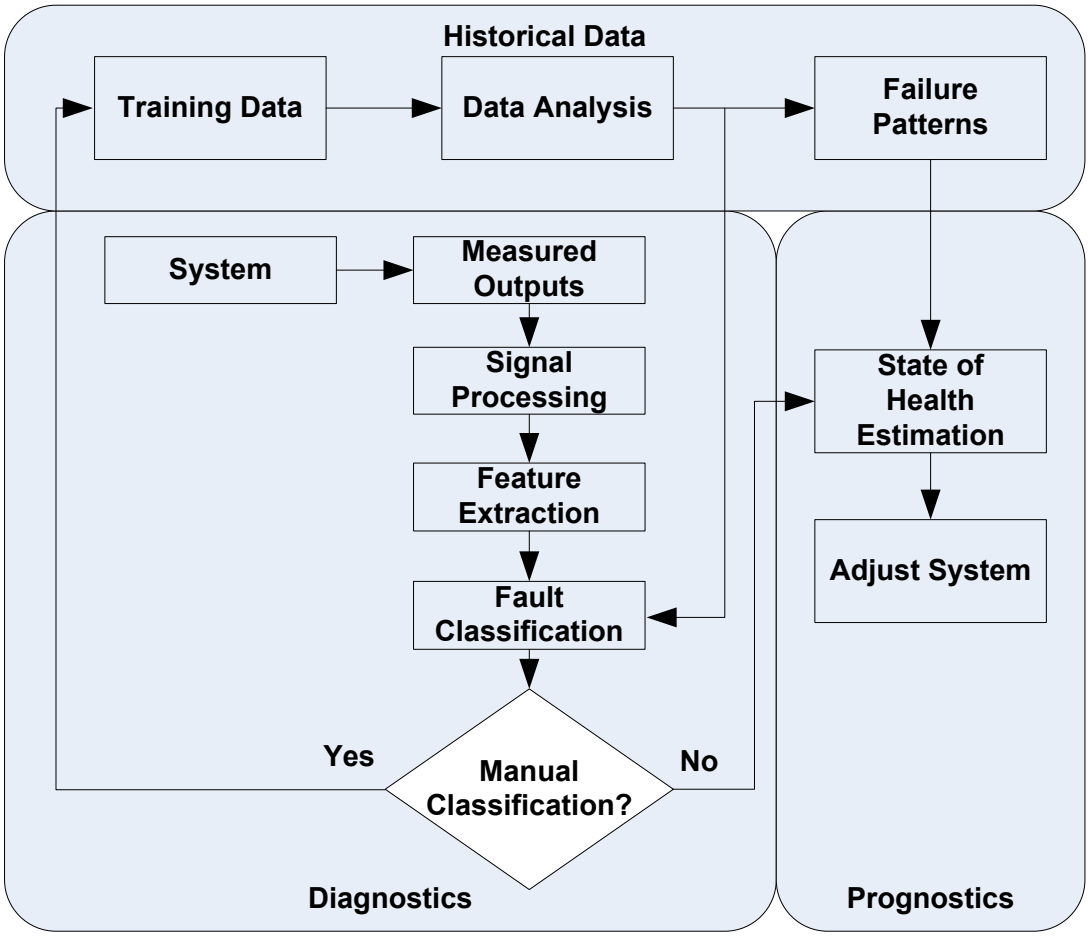


Figure 4.1: Prognostic Health Management Flow Chart

## 4.1 Preprocessing

Preprocessing improves the performance of data mining and machine learning. These processes cleanse, normalize, transform, or extract features from data. Data cleaning is the removal of incomplete, incorrect, and irrelevant data. This is important to prevent outliers from negatively effecting the training process. Normalization implies scaling and shifting of data, which prevents one feature from outweighing another. A transformation changes the axes a data set is plotted against. Principal component analysis and independent component analysis can transform the axes of data and reduce the number of axes (feature reduction). Feature reduction reduces the computational cost while possibly improving the effectiveness of a classifier. High dimensionality systems require significant data to effectively train, thus providing another advantage of reducing dimensionality.

### 4.1.1 Independent Component Analysis

Independent component analysis (ICA) is a technique to find directions on data that are most independent from each other. It is an expansion on blind source separation. FastICA is a package for MATLAB programmed at the Helsinki University of Technology [38]. It offers a computationally efficient method to determine the independent components in a data set. It works on a fixed-point iteration scheme to maximize non-Gaussianity.

The following is a brief summary and example of the fastICA algorithm. Please see [38] to gain a deeper understanding. To maximize the non-Gaussianity of the projection $\mathbf{w}^T\mathbf{x}$, of a given data set $\mathbf{x}$. Choose an initial weight vector $\mathbf{w}_p$.

$$\mathbf{w}_{p+1} = E\mathbf{x}g(\mathbf{w}^T\mathbf{x}) - Eg'(\mathbf{w}^T\mathbf{x})\mathbf{w} \tag{4.1}$$

$$\mathbf{w}_{new} = \frac{\mathbf{w}_{p+1}}{||\mathbf{w}_{p+1}||} \tag{4.2}$$

Repeat these steps until the non-Gaussianity has converged. The non-gaussianity cost function may be found at [38].

To give an example of the fastICA tool two sinusoidal signals are combined and then

seperated. Let

$$y_1 = sin(t) \tag{4.3}$$

$$y_2 = sin(3 * \pi * t) \tag{4.4}$$

and

$$ymix_1 = 0.6 * y_1 + 0.4 * y_2 \tag{4.5}$$

$$ymix_2 = 0.6 * y_1 + 0.8 * y_2 \tag{4.6}$$

In Figure 4.2a the original signals of a sinusoids are shown. In Figure 4.2b the two signals are combined with Equation 4.5 and Equation 4.6. In Figure 4.2c the original signals are decorrelated by fastICA with reasonable success. This example illustrates the capability the fastICA algorithm.

### 4.1.2 Principal Component Analysis

Principal component analysis (PCA) is an unsupervised orthogonal linear transformation that projects data onto a new coordinate system where the data with the greatest variance lies in the first coordinate and the least variance lies in the last coordinate. Since high dimensionality data cannot be visualized easily, or represented graphically, PCA becomes a powerful tool. It orders data in decreasing variance and allows a (lossy) compression of data by removing low variance data.

To perform PCA analysis, the data set is normalized by subtracting the mean ($\mu$). Then the covariance matrix is determined.

Assume the data set

$$[X, Y] = \begin{pmatrix} X_1 & Y_1 \\ X_2 & Y_2 \\ \vdots & \vdots \\ X_i & Y_i \end{pmatrix} \tag{4.7}$$

The mean is removed from the data

$$X_{norm,i} = X_i - \mu_x \tag{4.8}$$

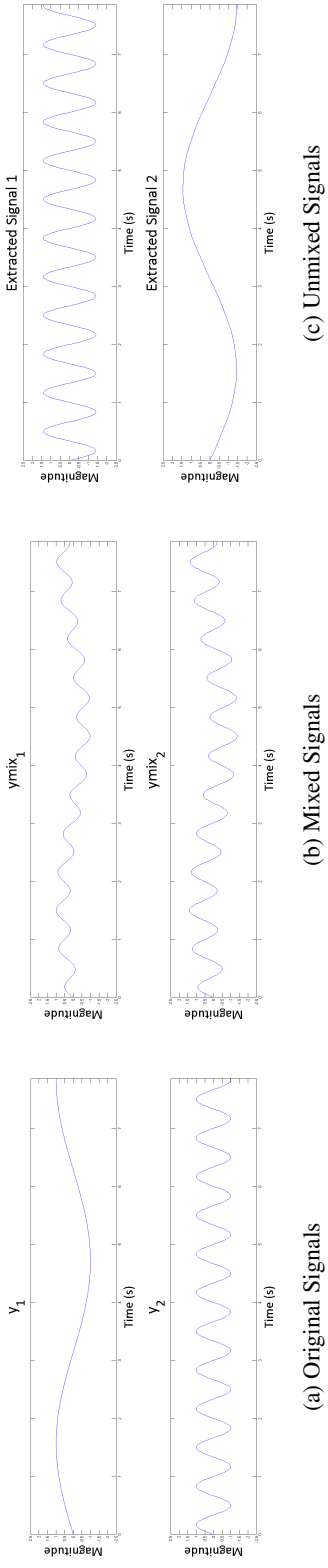


(a) Original Signals (b) Mixed Signals (c) Unmixed Signals

Figure 4.2: ICA Analysis

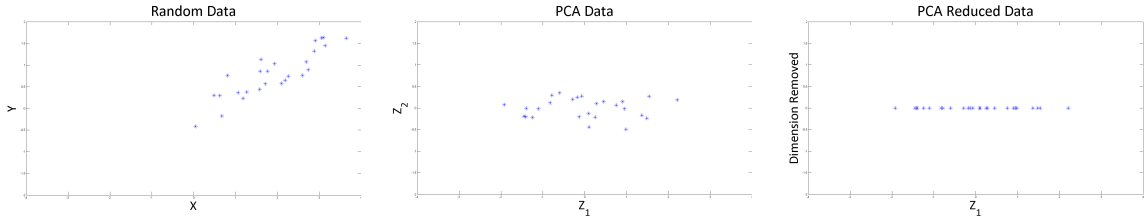


(a) Original Data (b) PCA Analyzed (c) Dimension Reduction

Figure 4.3: PCA Analysis

$$Y_{norm,i} = Y_i - \mu_y \tag{4.9}$$

Let $\mathbf{C}$ be the covariance of the normalized data set $[X, Y]$

$$\mathbf{C} = cov(X_{norm}, Y_{norm}) = \mathbf{E}[(X_{norm} - \mu_{x,norm})(Y_{norm} - \mu_{y,norm})] \tag{4.10}$$

The eigenvalues ($\lambda$) are determined from the covariance matrix

$$det(\mathbf{C} - \lambda\mathbf{I}) = 0 \tag{4.11}$$

and so are eigenvectors ($\mathbf{v}$)

$$(\mathbf{C} - \lambda\mathbf{I})\mathbf{v} = 0 \tag{4.12}$$

The eigenvectors are transposed and sorted by largest eigenvalue first to sort by most variance. The transformed data ($\mathbf{Z}$) is calculated by

$$\mathbf{Z} = \mathbf{v}' * [X_{norm} Y_{norm}]' \tag{4.13}$$

About 90% of the variance is typically kept when reducing the dimensionality. The equation below determines how many rows to keep, where $k$ is the number of rows required to meet the condition, while $n$ is all of the rows of the matrix.

$$0.9 >= \frac{\sum_i^k \lambda_i}{\sum_i^n \lambda_i} \tag{4.14}$$

An example of the transformation is presented in Figure 4.3 where random data is generated along a line, transformed, and reduced. Figure 4.3b shows the data along new axes that contain the most variance. Figure 4.3c reduces the dimensionality, maintaining at least

90% of the variance. The reduced dimensionality system simplifies a classification scheme by reducing the complexity of the boundaries.

## 4.2 Naïve Bayes Classifier

The Naïve Bayes classifier is a technique in pattern classification. Suppose we have a set $\Omega = \{\omega_1, \omega_2, ..., \omega_k\}$ of $K$ classes that are mutually exclusive. Their prior probability is defined by $P(\omega_k)$. Since the sum of the probabilities must equal one, we have the following equation.

$$\sum_{k=1}^{K} P(\omega_k) = 1 \tag{4.15}$$

A measurement vector $\mathbf{z}$ with dimension $N$ is produced by a sensory system. $p(\mathbf{z}|\omega_k)$ is the conditional probability density function of measurement vector $\mathbf{z}$. If an unknown class gives a measurement vector $\mathbf{z}$, its density is given by $p(\mathbf{z})$. Below, the unconditional density is derived from the conditional densities and weighting them by their prior probabilities.

$$p(\mathbf{z}) = \sum_{k=1}^{K} p(\mathbf{z}|\omega_k)P(\omega_k) \tag{4.16}$$

Bayes' theorem is used to determine the probability of a specific class ($\omega$) given a measurement vector ($\mathbf{z}$). This is written as

$$P(\omega_k|\mathbf{z}) = \frac{p(\mathbf{z}|\omega_k)P(\omega_k)}{p(\mathbf{z})} \tag{4.17}$$

The previous information, i.e. prior probabilities and conditional probabilities, is enough to design a basic classifier. However, to improve the classifier a cost function can be applied. A quantity called the conditional risk may be determined for assigning a class to a measurement vector. The conditional risk is determined by the expectation of the cost.

$$R(\hat{\omega}_i|\mathbf{z}) = E[C(\hat{\omega}_i|\omega_k)|\mathbf{z}] = \sum_{k=1}^{K} C(\hat{\omega}_i|\omega_k)P(\omega_k|\mathbf{z}) \tag{4.18}$$

The optimal classifier has the minimal risk. This is stated as:

$$\hat{\omega}_{BAYES}(\mathbf{z}) = \hat{\omega}_i \text{ such that: } R(\hat{\omega}_i|\mathbf{z}) \leq R(\hat{\omega}_j|\mathbf{z}) i, j = 1, 2, ..., K \tag{4.19}$$

To briefly express this

$$\hat{\omega}_{BAYES}(\mathbf{z}) = \underset{\omega \in \Omega}{\operatorname{argmin}}\{R(\omega|\mathbf{z})\} \tag{4.20}$$

Through a few substitutions the following is achieved

$$\hat{\omega}_{BAYES}(\mathbf{z}) = \underset{\omega \in \Omega}{\operatorname{argmin}}\{\sum_{k=1}^{K} C(\omega|\omega_k) p(\mathbf{z}|\omega_k) P(\omega_k)\} \tag{4.21}$$

This classification technique is called Bayesian Classification, or Minimum Risk Classification.

**MAP Classification**

If the cost function is uniform for a misclassified object, and zero cost when there is a correct classification, the bayes decision function becomes the maximum a posteriori probability classifier (MAP classifier). First, the cost function can be written with the Kronecker delta function $\delta(i, k)$ as

$$C(\hat{\omega}_i|\omega_k) = 1 - \delta(i, k) \text{ with: } \delta(i, k) = \begin{cases} 1 & \text{if } i = k \\ 0 & \text{elsewhere} \end{cases} \tag{4.22}$$

When this is incorporated into conditional risk, the maximization of the posterior probability $P(\hat{\omega}_i|\mathbf{z})$ is equivalent to the minimization of the risk. This creates the MAP classifier.

$$\hat{\omega}_{MAP}(\mathbf{z}) = \underset{\omega \in \Omega}{\operatorname{argmax}}\{P(\omega|\mathbf{z})\} \tag{4.23}$$

This can be rewritten in a more usable form as

$$\hat{\omega}_{MAP}(\mathbf{z}) = \underset{\omega \in \Omega}{\operatorname{argmax}}\{p(\mathbf{z}|\omega) P(\omega)\} \tag{4.24}$$

The Naïve Bayes classifier implemented with feature extraction from independent component analysis and principal component analysis represents a powerful tool in pattern

recognition. The features extracted represent the measurement vector ($\mathbf{z}$). Each class ($\omega$) represents a state of health for the enhanced automotive fuel cell model. These tools and their effectiveness are a focus of this research.

# Chapter 5

# Fuel Cell Fault Detection

A methodology is developed to determine the capability of a Naïve Bayes classifier for fuel cell fault classification. The feature enhanced automotive fuel cell model is used to generate data for a completely healthy stack at various humidification levels. The model is then used to create conditions where one cell is deteriorated by 1 to 10% in activation losses, ohmic losses, and concentration losses. For the purposes of this research only healthy stacks, activation losses, and ohmic losses are classified. Their features are selected and reduced when capable for classification.

## 5.1 Data Generation

The model, which consists of a 380 cell stack and a single modifiable cell, is driven under a polarization curve. It is necessary to run the model through a warm-up period near full power to remove any transient conditions such as its thermal load and membrane humidification. The model begins at a forty amp draw and over a ten minute ascension reaches a load of 200 amps. This is held for ten minutes. Following the warm up period is a standard polarization curve test. The current draw is reduced to thirty amps. As seen in Figure 5.1 the system is stepped regularly at every sixteen minutes. This is done until reaching a full power draw at 250 amps. The process repeats in the opposite direction and decreases to 30 amps. The polarization curve is tested in both directions because different transients occur.

The modifiable cell has adjustable gains for activation loss, ohmic loss, and concentration loss. The concentration loss region in a fuel cell is typically not reached in an automotive fuel cell environment. For this reason the focus of this research is in the activation loss and ohmic loss regions. The model is driven through the polarization curve

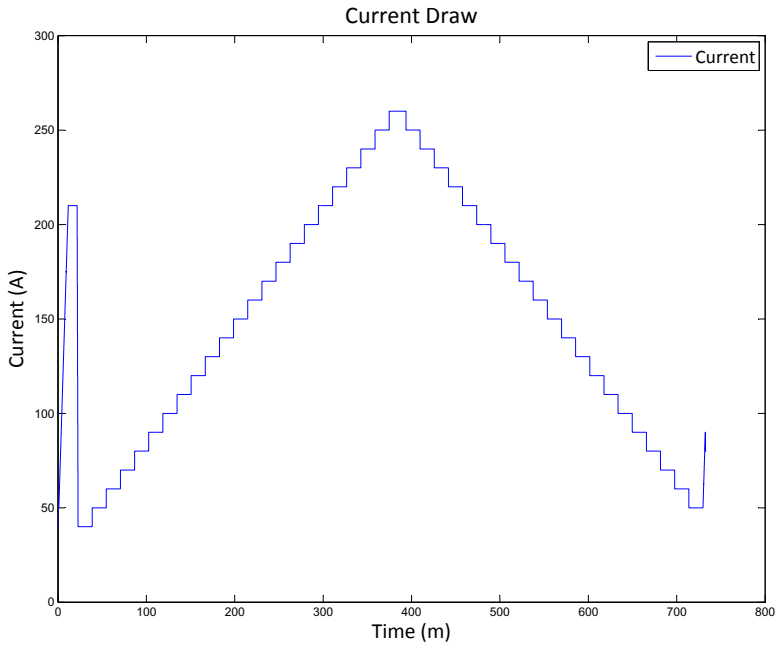


Figure 5.1: Fuel Cell System Current Draw

described previously while the gain is modified for each test. A healthy stack polarization curve with a damaged cell polarization curve is recorded with each test. The system outputs are also recorded. A target relative humidity is set with each operation. The stack maintains a higher temperature when a lesser relative humidity is desired.

Figure 5.2 demonstrates a full polarization curve including warm up and shut down periods. Polarization curves are displayed for several different states of health, these include healthy at 90% humidification, a 5% ohmic loss at 90% humidification, healthy at 83% humidification, and concentration loss at 83% humidification. The abnormal data in this plot is due to the warm up and cool down periods in the polarization curve test. Large step changes in current draw can drastically affect the fuel cell stack's voltage response. These are removed out in the next figure.

Figure 5.3 reduces the information to the polarization curve test. The equidistant spikes visible in this figure are due to thermal cycling and anode purging. The effects of reduced humidification, ohmic loss, and concentration loss are visible in this plot. The 90% humidified polarization curves mantain higher voltages than the reduced humidification curves.

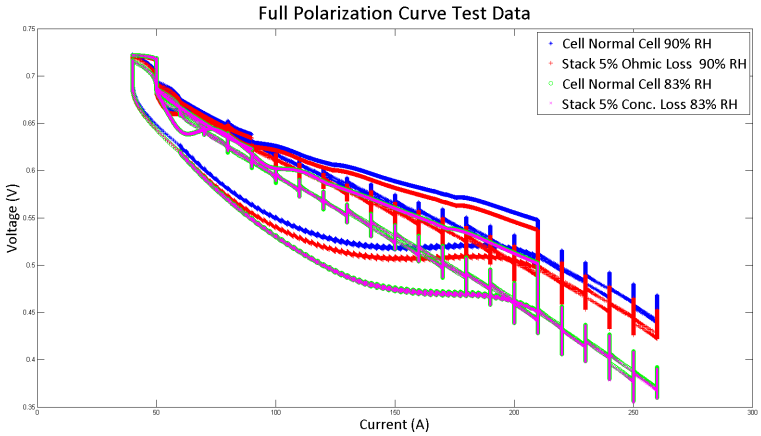


Figure 5.2: Full Polarization Curve Test Data Including Warmup and Shutdown

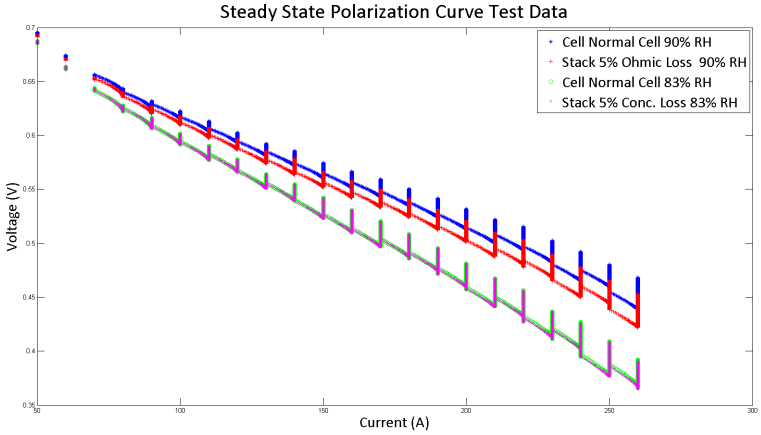


Figure 5.3: Polarization Curve Test Data with Warmup and Shutdown Removed

The healthy cell and 5% ohmic loss cell track well together at low current draw but separate towards higher currents. The 83% humidified curves track almost perfectly at low and medium current draw. The 5% concentration loss does not have the significant voltage drop like the ohmic loss.

A tremendous amount of information is available from the model. These outputs include compressor dynamics, membrane dynamics, thermal dynamics, controller outputs, inlet and outlet manifold dynamics for the cathode and anode, along with anode and cathode flow rates, stoichiometry, and pressures. Anode and cathode outputs are available from both the stack and the 'healthy' or 'damaged' cell.

Despite this high quantity of data, only several variables are of importance to this research. These variables are the ones commonly measured in an automotive fuel cell. The variables selected for data mining include the fuel cell voltage, the stack outlet coolant temperature, the stack cathode relative humidity, current draw, and whether or not the anode manifold is purging.

The type of data collected and the current steps implemented would likely be a service test taken after a set amount of hours of operation. Just like a vehicle has a set period of miles between oil changes, a service inspection could be set after a set number of operational hours. This inspection would monitor the previously described set of outputs and process them for classification.

The healthy test data records the stack outputs and the voltage from the single healthy cell separated from the healthy stack. The activation loss modifier and ohmic loss modifier are kept at a nominal value of one. The targeted humidification is kept at 90% humidity. The activation loss test data is generated with a single cell experiencing a greater activation loss, while the remaining 380 cells remain nominal. This setup should not significantly effect system outputs. This same procedure is repeated for the ohmic loss test data.

## 5.2 Data Processing

The data processed comes from the feature enhanced automotive fuel cell, but future implementation of these techniques should be applied to actual fuel cell data. Any fuel cell data analyzed will need to include what the failure mode is of each failed cell in a stack. This will require a post mortem analysis of the assembly. The data obtained from these analyses would replace the simulated data used in training.

### 5.2.1 Pre-processing

The preprocessing techniques require the healthy and unhealthy data in the same signal to determine the necessary transformations. This creates a plot similar to Figure 5.4. The plot consists of a healthy stack and healthy cell, appended by a healthy stack with an activation loss cell, appended by another healthy stack with an ohmic loss cell. The same current load

is applied to each simulation.

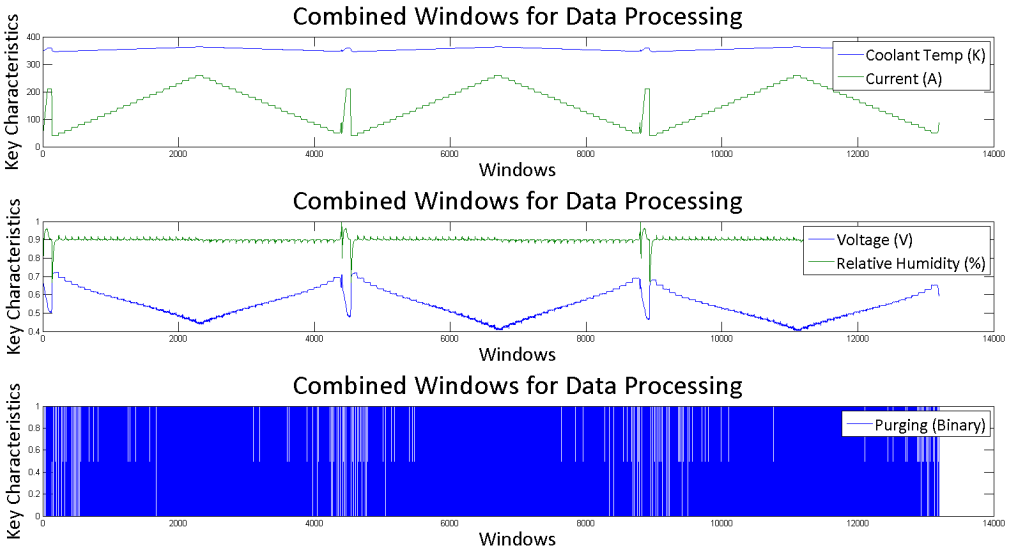


Figure 5.4: Combined Windowed data before preprocessing techniques are applied.

The data is processed by generating 'windows.' Each window is a snapshot of a set period of time. For this research a ten second rectangular window is used. The windows do not overlap. If frequency data is needed (perhaps while analyzing transients) a different windowing technique may be required. Under these circumstances the windows may even overlap to avoid missing information.

This model is not calculated through a fixed time step analysis, so each ten second window may contain more or less data points than another window. A uniform feature set is created by averaging each of the values collected from the window. This feature set ($\mathbf{z}$) represents a five dimensional point.

$$\mathbf{z} = \begin{pmatrix} \mathbf{E}(V) & \mathbf{E}(T_{fc,clt}) & \mathbf{E}(\phi_c) & \mathbf{E}(I) & \mathbf{E}(P_b) \end{pmatrix} \tag{5.1}$$

This research is focused on steady state fuel cell data. Each window must be selected to specifically target steady state. An example of a non-steady state window is located in Figure 5.5a and a steady state window is presented in Figure 5.5b. The input current is known and the windows can be related to this information. Each current step allowed 16 minutes

of settling time. These 960 seconds create 96 windows. The first two windows are ignored while the remaining 94 windows from each step are used for training and classification. This implies some voltage swing from the thermal system because it has not yet reached steady state, but the fastest transients have occurred. Throughout this time period multiple anode purges will occur effecting fuel cell voltages and temperatures.

The Naïve Bayes classifier could be implemented at this point but further pre-processing through ICA or PCA, as shown in Chapter 4, may be beneficial. Implementing the fastICA algorithm iteratively searches for the most independent signals possible. The iterative search begins with randomly selected weights and continues until the non-gaussianity is maximized. This can create slightly different transformation matrices on each use of the fastICA algorithm. The different transformation matrices did not significantly impact classification results (+/- $0.5\%$).

The entire data set is brought through indepedent component analysis. The ICA technique removes the mixed signals and creates an output seen in Figure 5.6. The data presented no longer represents anything in physical units and can only be referenced by channel or feature. However, it could be presumed that Feature 2 represents the signal from current and Feature 4 represents the purging signal. The transformed data is presented to the Naïve Bayes classifier to create prior probabilities for each class. This will be discussed later.

Principal component analysis is also investigated. Figure 5.7 through Figure 5.11 show the implementation on the same set of data. These features are ordered by their variance.

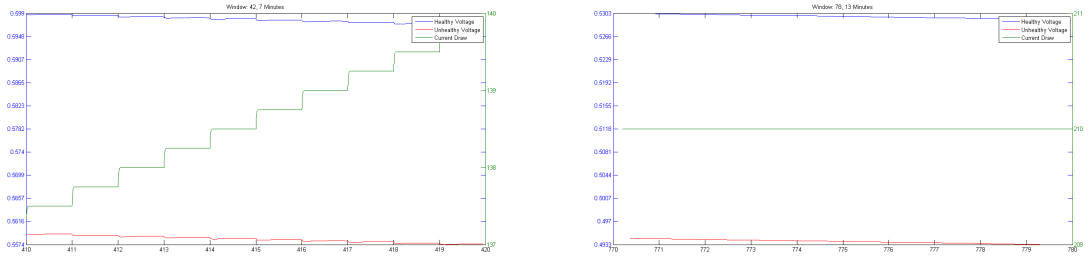


(a) Non-steady State Window

(b) Steady State Window

Figure 5.5: Comparison of 10 Second Windows between Steady State and Non Steady Current Draws

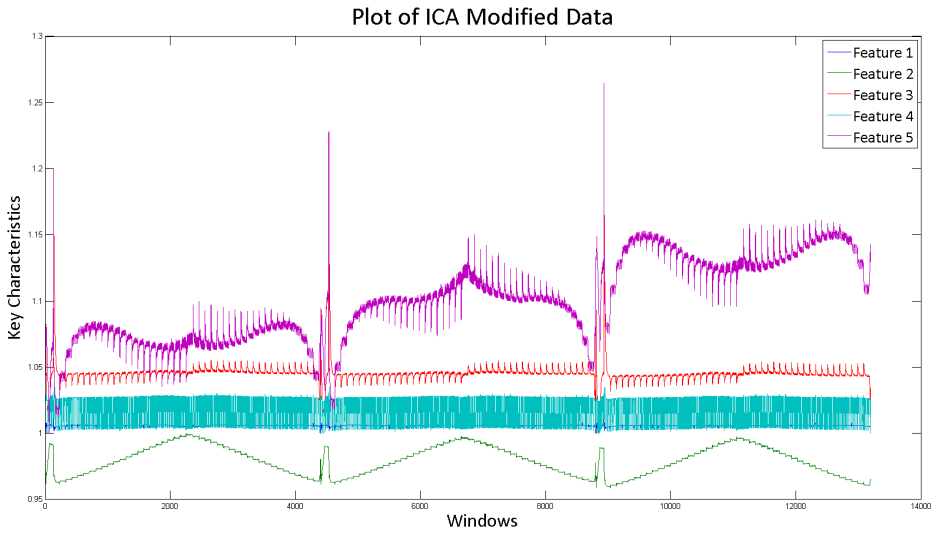


Figure 5.6: Independent Component Analysis Modified Data

Feature 1 has the most variance, followed by Feature 2, and so on. This information can be used when applying dimensionality reduction. Although the first feature may have the most variance it does not imply it is most related to health classification. The amount of variance is determined by the eigenvalues which are displayed in Table 5.1. Feature 1 dominates the variance of the data. Upon examining Figure 5.7 it appears highly correlated with the purging operation due to its extremely high rate of oscillation and consistent magnitude.

The remaining features have less and less variance. Features 3 and 4 have small eigenvalues, and feature 5 is almost negligible. PCA is sensitive to the magnitude of the signals, possibly ranking less important features first. Applying different normalization schemes may improve the feature weighting and feature reduction.

The transformed data set generated by principal component analysis is used as the feature set in the Naïve Bayes classifier.

| Data | Eigenvalue | % Variance |
|---|---|---|
| Feature 1 | $2.31341 * 10^{-1}$ | 76.64% |
| Feature 2 | $6.95776 * 10^{-2}$ | 23.05% |
| Feature 3 | $7.21272 * 10^{-4}$ | 00.23% |
| Feature 4 | $2.13798 * 10^{-4}$ | 00.07% |
| Feature 5 | $6.01549 * 10^{-7}$ | 00.00% |

Table 5.1: Principal Component Eigenvalues Calculated by Equation 4.11

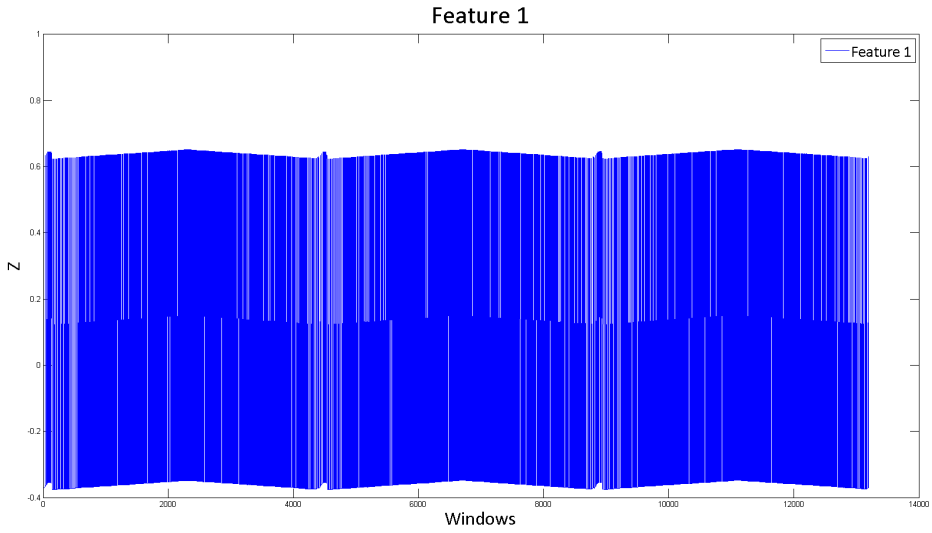


Figure 5.7: Principal Component Analysis Modified Data: Feature 1

## 5.3 Naïve Bayes Classification

Each of the scenarios stated in the Data Processing section provide a different set of data to analyze in the Naïve Bayes classifier. These scenarios include: no preprocessing, PCA preprocessing, and ICA preprocessing. The implementation of PCA allows for dimensionality reduction and an analysis of the variance of each feature. These features are presented to the Naïve Bayes classifier for training. The classifier assumes a normal gaussian distribution for each class. Alternative distributions are possible to create a non-gaussian Naïve Bayes classifier. A mean and variance are calculated for each feature of each state of health (healthy, activation loss, ohmic loss). These values are calculated from the training windows supplied. Of the 94 windows used per current step, 47 are used for training with the other 47 used for validation.

The variance and mean of each feature for each validation window are calculated. Their probability of belonging to each class given each feature is determined. The classifier does not weight one class more than another. The prior probabilities are equally split, with three cases each prior probability is $1/3$. Future work could modify the prior probability based upon the age of the fuel cell and other available information. As discussed earlier, this becomes a subset of the Naïve Bayes classifier, a MAP classifier. This implies the cost

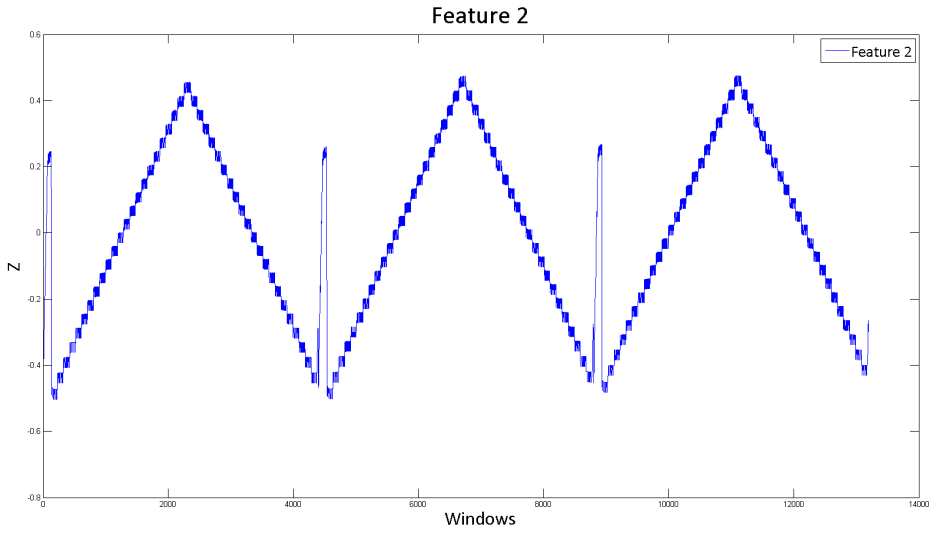


Figure 5.8: Principal Component Analysis Modified Data: Feature 2

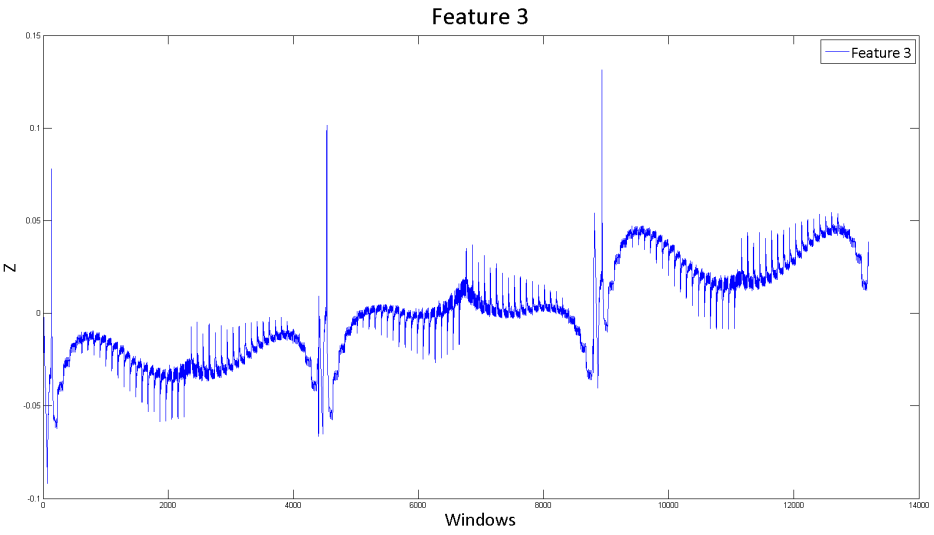


Figure 5.9: Principal Component Analysis Modified Data: Feature 3

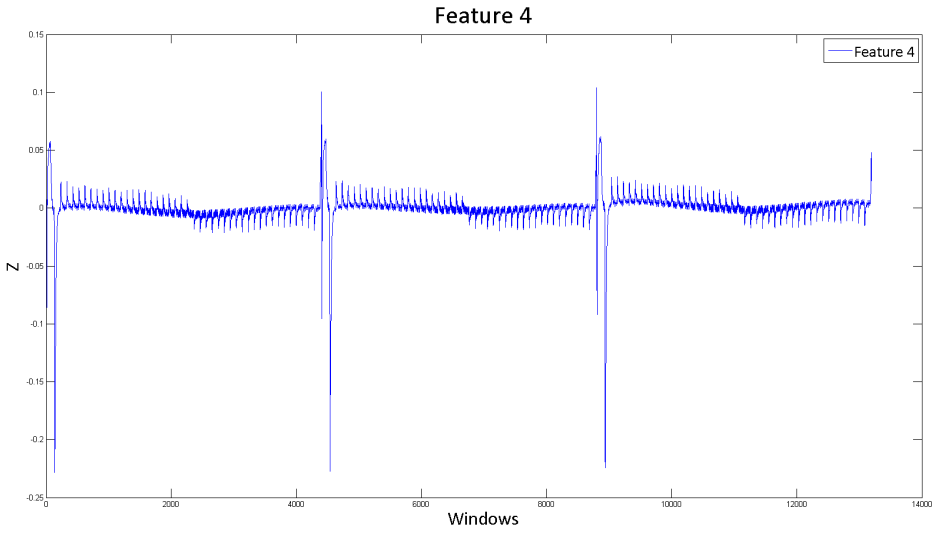


Figure 5.10: Principal Component Analysis Modified Data: Feature 4

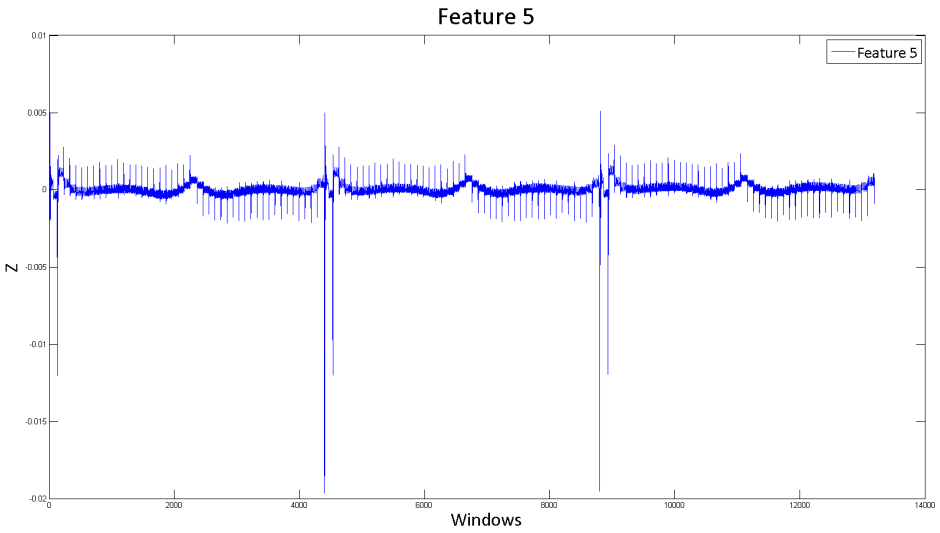


Figure 5.11: Principal Component Analysis Modified Data: Feature 5

function is the identity matrix. The probability of the window belonging to each class is compared and the highest probability class is selected. The results of the validation data are presented in the following tables.

The results of no preprocessing are presented in Table 5.2. The headings represent the states: healthy, activation loss, and ohmic loss. In the no preprocessing scenario the values from cell voltage, coolant, relative humidity, stack current, and purging are are normalized before their means and variances are determined. The results are not promising. A failing three class classification method would statistically offer a 33% success rate. In both healthy and activation loss classifications the classifier fails to choose the correct state of health. All three classification attempts choose the ohmic loss region. This makes the correct decision for the ohmic loss region questionable.

| | | Classified Health | | |
|---|---|---|---|---|
| | | H | A | O |
| Modeled Health | H | 28.00% | 28.04% | 43.96% |
| | A | 24.73% | 22.26% | 53.01% |
| | O | 22.36% | 13.45% | 64.19% |

Table 5.2: Five Feature No Preprocessing Bayes Classifier Results on 10% Losses

| | | Classified Health | | |
|---|---|---|---|---|
| | | H | A | O |
| Modeled Health | H | 93.84% | 06.16% | 00.00% |
| | A | 14.16% | 79.44% | 06.40% |
| | O | 00.85% | 07.15% | 91.99% |

Table 5.3: Five Feature ICA Preprocessed Bayes' Classifier Results on 10% Losses

| | | Classified Health | | |
|---|---|---|---|---|
| | | H | A | O |
| Modeled Health | H | 84.32% | 15.68% | 00.00% |
| | A | 15.63% | 76.03% | 08.34% |
| | O | 02.13% | 06.87% | 91.00% |

Table 5.4: Five Feature ICA Preprocessed Bayes' Classifier Results on 7% Losses

Table 5.3 through Table 5.5 demonstrate the capability of the ICA technique. By implementing the data mining technique the success rate of classification improved to an

| | | Classified Health | | |
|---|---|---|---|---|
| | | H | A | O |
| Modeled Health | H | 73.99% | 25.68% | 00.33% |
| | A | 16.82% | 70.01% | 13.17% |
| | O | 05.45% | 06.16% | 88.39% |

Table 5.5: Five Feature ICA Preprocessed Bayes' Classifier Results on 5% Losses

exceptional level. The classification of each state of health is successful when identifying the healthy, 10% activation loss, and 10% ohmic loss states. This classification is repeated with 7% losses and 5% losses. In all cases the results are promising. It is noted that as the losses deviate further from healthy, the classification results become more successful. This is understandable as the mean of each feature departs from state of health to state of health. This is visible in Figure 5.6.

| | | Classified Health | | |
|---|---|---|---|---|
| | | H | A | O |
| Modeled Health | H | 87.02% | 12.98% | 00.00% |
| | A | 11.80% | 85.93% | 02.27% |
| | O | 00.00% | 10.99% | 89.01% |

Table 5.6: Five Feature PCA Preprocessed Bayes' Classifier Results on 10% Losses

| | | Classified Health | | |
|---|---|---|---|---|
| | | H | A | O |
| Modeled Health | H | 74.66% | 25.25% | 00.09% |
| | A | 13.07% | 83.66% | 03.27% |
| | O | 01.94% | 22.55% | 75.51% |

Table 5.7: Five Feature PCA Preprocessed Bayes' Classifier Results on 7% Losses

Principal component analysis is also investigated for its pre-processing ability. Table 5.6 through Table 5.8 show the classification success rate without feature reduction. Again, this is very successful in comparison to no preprocessing. The results are comparable with the ICA preprocessing results. However, classification appears more consistent with PCA than ICA. ICA successfully identified healthy cells at a 94% sucess rate while PCA only obtained 87%, but ICA only identified an activation loss correctly 80% of the time as opposed to PCA identifying activation loss correctly 85% of the time. This consistency

| | | Classified Health | | |
|---|---|---|---|---|
| | | H | A | O |
| Modeled Health | H | 67.79% | 31.45% | 00.76% |
| | A | 14.54% | 77.78% | 07.67% |
| | O | 02.65% | 30.13% | 67.22% |

Table 5.8: Five Feature PCA Preprocessed Bayes' Classifier Results on 5% Losses

continues as the losses become more negligible. The trend of increasing success rates with increasing losses is also consistent across all three classifications.

| | | Classified Health | | |
|---|---|---|---|---|
| | | H | A | O |
| Modeled Health | H | 86.93% | 13.07% | 00.00% |
| | A | 12.08% | 85.60% | 02.32% |
| | O | 00.00% | 11.23% | 88.77% |

Table 5.9: Three Feature PCA Preprocessed Bayes' Classifier Results on 10% Losses

| | | Classified Health | | |
|---|---|---|---|---|
| | | H | A | O |
| Modeled Health | H | 75.94% | 24.02% | 00.05% |
| | A | 12.08% | 81.24% | 04.88% |
| | O | 01.94% | 21.51% | 76.55% |

Table 5.10: Three Feature PCA Preprocessed Bayes' Classifier Results on 7% Losses

PCA is capable of reducing features based on their amount of variance. Features with the largest variance are kept and those with the least are removed. The number of features retained is determined by selecting the number of rows desired, or by calculating a desired percentage of variance from the original data set to keep. Reducing the number of features in analysis simplifies the classification system and reduces computational power. This is particularly important when the number of features can reach the hundreds. An example of this is the reduction of fourier transform coefficients.

The results of the Naïve Bayes classifier on reduced feature sets are shown in Table 5.9 through Table 5.11. The three feature classification rate at 10% losses are slightly below the five feature classification results, but only by approximately 1%. As noted before the success rate of the classifier increases as the percentage loss increases from nominal. Healthy

| | | Classified Health | | |
|---|---|---|---|---|
| | | H | A | O |
| Modeled Health | H | 71.34% | 26.58% | 02.08% |
| | A | 18.85% | 69.68% | 11.46% |
| | O | 03.88% | 26.76% | 69.35% |

Table 5.11: Three Feature PCA Preprocessed Bayes' Classifier Results on 5% Losses

classifications succeed almost 87% of the time with a 10% loss compared to just 71% of the tiem at a 5% loss.

## 5.4 Conclusion

The enhanced automotive fuel cell model developed in this research provided an effective tool for developing fault recognition techniques on proton exchange membrane fuel cell technology. This research effectively incorporated cell deviation for analyzing a single cell. The single cell model tracks with negligible error (on the order of $10^{-7}$) in nominal conditions. The charge double layer completes the dynamic electrical effects in the enhanced model. The addition of a thermal model introduces long term transients as the stack is no longer idealized at $80°$C. The control of cathode humidification by manipulating the thermal model's target temperature effectively prevents liquid water from forming in the cathode channels. Inert gas build-up due to nitrogen permeation and impure fuel sources is successfully modeled, reducing the output voltage as the nitrogen accumulates. The anode outlet manifold successfully models the purging transients, introducing yet another automotive fuel cell transient. Each of these effects have the ability to increase and decrease the operational fuel cell voltage making fuel cell fault classification more complicated.

The Naïve Bayes classifier successfully identified the faults of activation losses and increased ohmic losses on the enhanced automotive fuel cell model. The classifier requires preprocessing to the recorded outputs to obtain correct classifications. Independent component analysis through the fastICA algorithm and principal component analysis both proved to be successful tools in data preprocessing. Their classification performance is not significantly different. As the faults grew from nominal, the success rate of the classifier

improved.

### 5.4.1 Future Work

The enhanced automotive fuel cell model opens an array of new research opportunities, both within the model itself and for additional fault classification. The enhanced model may be used to study more control techniques, particularly for anode purging. The system could benefit from optimization techniques. A continuous purge system could be implemented in its place to compare effects. The feed forward fuel controls could also be adjusted to minimize voltage drop during a purge event.

The thermal model also lends itself to some possible improvements. These include the incorporation of anode and cathode convection within their volumes. The bypass valve controls could also be improved to adjust in advance to changes in power draw. The effect of a pump should also be included in the parasitic losses of the system.

Nitrogen is only one of the permeable gases. Fuel crossover does occur as hydrogen can permeate from anode to cathode. Oxygen permeation from cathode to anode occurs as well, instantly reacting with hydrogen to produce water without generating useful power.

As more information becomes available the membrane humidification model can be enhanced to account for membrane water uptake. The model currently calculates membrane humidification as a function of cathode and anode humidification and doesnt account for the uptake transient.

Additional research can continue without further model enhancements for state of health classification as well. The more complicated system opens a variety of adjustable parameters for future faults. The scope of this work detected a difference between cells in different health states, but a more complex classification system should be capable of discerning fuel cell faults from balance of plant faults. The classifier complexity can also take into account different prior probabilities, or priors that change with fuel cell operation. Different probabilities may also be investigated for each feature to more accurately describe each feature's distribution. Exciting opportunities exist to further the research in both the enhanced automotive fuel cell model and the fault recognition techniques applied in this research.

# Bibliography

[1] J. Larminie and A. Dicks, *Fuel Cell Systems Explained*. 2008.

[2] R. Meyer and B. Yao, "Control of a PEM fuel cell cooling system," in *Proc. of IMECE*, vol. 14151, Citeseer, 2006.

[3] J. T. Pukrushpan, H. Peng, and A. G. Stefanopoulou, "Control-Oriented Modeling and Analysis for Automotive Fuel Cell Systems," *Journal of Dynamic Systems, Measurement, and Control*, vol. 126, no. 1, p. 14, 2004.

[4] J. T. Pukrushpan, A. G. Stefanopoulou, and H. Peng, *Control of Fuel Cell Power Systems: Principles, Modeling, Analysis and Feedback Design*. Springer, 2005.

[5] R. Othman, A. L. Dicks, and Z. Zhu, "Non precious metal catalysts for the PEM fuel cell cathode," *International Journal of Hydrogen Energy*, vol. 37, pp. 357–372, Jan. 2012.

[6] C. W. Bezerra, L. Zhang, H. Liu, K. Lee, A. L. Marques, E. P. Marques, H. Wang, and J. Zhang, "A review of heat-treatment effects on activity and stability of PEM fuel cell catalysts for oxygen reduction reaction," *Journal of Power Sources*, vol. 173, pp. 891–908, Nov. 2007.

[7] X. Li and I. Sabir, "Review of bipolar plates in PEM fuel cells: Flow-field designs," *International Journal of Hydrogen Energy*, vol. 30, pp. 359–371, Mar. 2005.

[8] S. Asghari, M. Shahsamandi, and M. Ashraf Khorasani, "Design and manufacturing of end plates of a 5kW PEM fuel cell," *International Journal of Hydrogen Energy*, vol. 35, pp. 9291–9297, Sept. 2010.

[9] J. Pukrushpan, *Modeling and control of fuel cell systems and fuel processors*. PhD thesis, The University of Michigan, 2003.

[10] B. J. Kim and M. S. Kim, "Studies on the cathode humidification by exhaust gas recirculation for PEM fuel cell," *International Journal of Hydrogen Energy*, vol. 37, pp. 4290–4299, Mar. 2012.

[11] A. Holland, *Integrated Systems, Design and Technology 2010: Knowledge Transfer in New Technologies*. 2011.

[12] Y. Tang, W. Yuan, M. Pan, and Z. Wan, "Experimental investigation on the dynamic performance of a hybrid PEM fuel cell/battery system for lightweight electric vehicle application," *Applied Energy*, vol. 88, pp. 68–76, Jan. 2011.

[13] N. Yousfisteiner, P. Mocoteguy, D. Candusso, D. Hissel, a. Hernandez, and a. Aslanides, "A review on PEM voltage degradation associated with water management: Impacts, influent factors and characterization," *Journal of Power Sources*, vol. 183, pp. 260–274, Aug. 2008.

[14] S. D. Knights, K. M. Colbow, J. St-Pierre, and D. P. Wilkinson, "Aging mechanisms and lifetime of PEFC and DMFC," *Journal of Power Sources*, vol. 127, pp. 127–134, Mar. 2004.

[15] X. Cheng, Z. Shi, N. Glass, L. Zhang, J. Zhang, D. Song, Z. Liu, H. Wang, and J. Shen, "A review of PEM hydrogen fuel cell contamination: Impacts, mechanisms, and mitigation," *Journal of Power Sources*, vol. 165, pp. 739–756, Mar. 2007.

[16] S. Zhang, X.-Z. Yuan, J. N. C. Hin, H. Wang, K. A. Friedrich, and M. Schulze, "A review of platinum-based catalyst layer degradation in proton exchange membrane fuel cells," *Journal of Power Sources*, vol. 194, pp. 588–600, Dec. 2009.

[17] H. Karimäki, L. Pérez, K. Nikiforow, T. Keränen, J. Viitakangas, and J. Ihonen, "The use of on-line hydrogen sensor for studying inert gas effects and nitrogen crossover in PEMFC system," *International Journal of Hydrogen Energy*, vol. 36, pp. 10179–10187, Aug. 2011.

[18] N. Yousfi-Steiner, P. Moçotéguy, D. Candusso, and D. Hissel, "A review on polymer electrolyte membrane fuel cell catalyst degradation and starvation issues: Causes, consequences and diagnostic for mitigation," *Journal of Power Sources*, vol. 194, pp. 130–145, Oct. 2009.

[19] T. Pokphet and W. Khan-ngern, "Effect of hydrogen Purging period on system performance of PEMFC," in *The 2010 International Conference on Electrical Engineering/Electronics. Computer. Telecommunications and Information Technology*, 2010.

[20] J. Wu, X. Z. Yuan, J. J. Martin, H. Wang, J. Zhang, J. Shen, S. Wu, and W. Merida, "A review of PEM fuel cell durability: Degradation mechanisms and mitigation strategies," *Journal of Power Sources*, vol. 184, pp. 104–119, Sept. 2008.

[21] R. Solasi, Y. Zou, X. Huang, K. Reifsnider, and D. Condit, "On mechanical behavior and in-plane modeling of constrained PEM fuel cell membranes subjected to hydration and temperature cycles," *Journal of Power Sources*, vol. 167, pp. 366–377, May 2007.

[22] B. Avasarala, R. Moore, and P. Haldar, "Surface oxidation of carbon supports due to potential cycling under PEM fuel cell conditions," *Electrochimica Acta*, vol. 55, pp. 4765–4771, June 2010.

[23] R. O. Duda, P. E. Hart, and D. G. Stork, *Pattern Classification*. John Wiley & Sons, 2001.

[24] J. Kim, I. Lee, Y. Tak, and B. Cho, "State-of-health diagnosis based on hamming neural network using output voltage pattern recognition for a PEM fuel cell," *International Journal of Hydrogen Energy*, pp. 1–10, Dec. 2011.

[25] R. Onanena, L. Oukhellou, D. Candusso, F. Harel, D. Hissel, and P. Aknin, "Fuel cells static and dynamic characterizations as tools for the estimation of their ageing time," *International Journal of Hydrogen Energy*, vol. 36, pp. 1730–1739, Jan. 2011.

[26] N. Y. Steiner, D. Hissel, P. Moçotéguy, and D. Candusso, "Non intrusive diagnosis of polymer electrolyte fuel cells by wavelet packet transform," *International Journal of Hydrogen Energy*, vol. 36, pp. 740–746, Jan. 2011.

[27] N. Yousfi Steiner, D. Hissel, P. Moçotéguy, and D. Candusso, "Diagnosis of polymer electrolyte fuel cells failure modes (flooding & drying out) by neural networks modeling," *International Journal of Hydrogen Energy*, vol. 36, pp. 3067–3075, Feb. 2011.

[28] M. Tanrioven and M. Alam, "Reliability modeling and analysis of stand-alone PEM fuel cell power plants," *Renewable Energy*, vol. 31, pp. 915–933, June 2006.

[29] N. Fouquet, C. Doulet, C. Nouillant, G. Dauphin-Tanguy, and B. Ould-Bouamama, "Model based PEM fuel cell state-of-health monitoring via ac impedance measurements," *Journal of Power Sources*, vol. 159, pp. 905–913, Sept. 2006.

[30] J. Wu, X. Yuan, H. Wang, M. Blanco, J. Martin, and J. Zhang, "Diagnostic tools in PEM fuel cell research: Part I Electrochemical techniques," *International Journal of Hydrogen Energy*, vol. 33, pp. 1735–1746, Mar. 2008.

[31] J. Wu, X. Ziyuan, H. Wang, M. Blanco, J. Martin, and J. Zhang, "Diagnostic tools in PEM fuel cell research: Part IIPhysical/chemical methods," *International Journal of Hydrogen Energy*, vol. 33, pp. 1747–1757, Mar. 2008.

[32] J. C. Amphlett, R. M. Baumert, R. F. Mann, B. A. Peppley, and P. R. Roberge, "Performance Modeling of the Ballard Mark IV Solid Polymer Electrolyte Fuel Cell," *Electrochemical Science and Technology*, vol. 142, no. 1, 1995.

[33] G. Vasu and a.K. Tangirala, "Control-orientated thermal model for proton-exchange membrane fuel cell systems," *Journal of Power Sources*, vol. 183, pp. 98–108, Aug. 2008.

[34] R. Ahluwalia and X. Wang, "Buildup of nitrogen in direct hydrogen polymer-electrolyte fuel cell stacks," *Journal of Power Sources*, vol. 171, pp. 63–71, Sept. 2007.

[35] R. Meyer and B. Yao, "Modeling and Simulation of a Modern PEM fuel cell System," *Proceedings of the 4th International Conference on Fuel Cell Science, Engineering and Technology*, 2006.

[36] Z. Chen and C. Lu, "Humidity sensors: a review of materials and mechanisms," *Sensor Letters*, vol. 3, pp. 274–295, 2005.

[37] J. Sun, H. Zuo, W. Wang, and M. G. Pecht, "Application of a state space modeling technique to system prognostics based on a health index for condition-based maintenance," *Mechanical Systems and Signal Processing*, vol. 28, pp. 585–596, Apr. 2012.

[38] A. Hyvärinen, "Fast and robust fixed-point algorithms for independent component analysis.," *IEEE transactions on neural networks / a publication of the IEEE Neural Networks Council*, vol. 10, pp. 626–34, Jan. 1999.

# Appendix A

# Miscellanous Parameters

| Parameter | Value | Units |
|---|---|---|
| $R_a$ | 286.9 | J/(kg K) |
| $p_a$ | 1.23 | kg/m$^3$ |
| $d_c$ | 0.2286 | m |

Table A.1: Compressor map parameters

| Parameter | Value |
|---|---|
| $a_0$ | $2.21195 * 10^{-3}$ |
| $a_1$ | $-4.63685 * 10^{-5}$ |
| $a_2$ | $-5.36235 * 10^{-4}$ |
| $a_3$ | $2.70399 * 10^{-4}$ |
| $a_4$ | $-3.69906 * 10^{-5}$ |
| $b_0$ | $2.44419$ |
| $b_1$ | $-1.34837$ |
| $b_2$ | $1.76567$ |
| $c_0$ | $0.43331$ |
| $c_1$ | $-0.68344$ |
| $c_2$ | $0.80121$ |
| $c_3$ | $-0.42937$ |
| $c_4$ | $0.10581$ |
| $c_5$ | $-9.78755 * 10^{-3}$ |

Table A.2: Compressor map regression coefficients

| Parameter | Value | Units |
|---|---|---|
| $k_v$ | 0.0153 | V/(Rad/s) |
| $k_t$ | 0.0153 | N-m/A |
| $R_{cm}$ | 0.82 | $\Omega$ |
| $\eta_{cm}$ | 98 | $\%$ |

Table A.3: Compressor motor parameters

| Parameter | Value | Units |
|---|---|---|
| $p_{atm}$ | 101.325 | kPa |
| $T_{atm}$ | 298.15 | K |
| $\gamma_{air}$ | 1.4 | |
| $C_{p,air}$ | 1004 | J/(mol K) |
| $\rho_{air}$ | 1.23 | kg/m$^3$ |
| $\bar{R}$ | 8.3145 | J/(mol K) |
| $R_{air}$ | 286.9 | J/(mol K) |
| $R_{H_2}$ | 4124.3 | J/(mol K) |
| $R_{N_2}$ | 296.8 | J/(mol K) |
| $R_{O_2}$ | 259.8 | J/(mol K) |
| $R_v$ | 461.5 | J/(mol K) |
| $M_{H_2}$ | $2.016 * 10^{-3}$ | kg/mol |
| $M_{N_2}$ | $28 * 10^{-3}$ | kg/mol |
| $M_{O_2}$ | $31 * 10^{-3}$ | kg/mol |
| $M_v$ | $18.02 * 10^{-3}$ | kg/mol |
| $F$ | 96485 | Coulombs |

Table A.4: Thermodynamic constants in base model

| Parameter | Value | Units |
|---|---|---|
| $p_{membr,dry}$ | 0.002 | kg/cm$^3$ |
| $M_{membr,dry}$ | 1.1 | kg/mol |
| $t_{membr}$ | 0.01275 | cm |
| $N_{fc}$ | 381 | |
| $A_{fc}$ | 280 | cm$^2$ |
| $J_{cp}$ | $5 * 10^{-5}$ | kg m$^2$ |
| $V_a$ | 0.005 | m$^3$ |
| $V_c$ | 0.01 | m$^3$ |
| $V_{sm}$ | 0.02 | m$^3$ |
| $V_{rm,a}$ | 0.005 | m$^3$ |
| $V_{rm,c}$ | 0.005 | m$^3$ |
| $CD_{rm,a}$ | 0.0124 | |
| $CD_{rm,c}$ | 0.0124 | |
| $A_{T,rm,a}$ | 0.002/450 | m$^2$ |
| $A_{T,rm,c}$ | 0.002 | m$^2$ |
| $k_{sm,o}$ | $0.3629 * 10^{-3}$ | kg/(s Pa) |
| $k_{a,o}$ | $0.2177 * 10^{-3}$ | kg/(s Pa) |
| $k_{c,o}$ | $0.2177 * 10^{-3}$ | kg/(s Pa) |

Table A.5: Fuel cell component parameters

| Parameter | Value | Units |
|---|---|---|
| $C_{v,air}$ @ $65°C$ | 717.8 | J/(kg K) |
| $C_{v,clt}$ @ $65°C$ | 395 | J/(kg K) |
| $C_{v,fc}$ | 1000 | J/(kg K) |
| $C_{v,hex}$ | 1000 | J/(kg K) |
| $h_{c,clt,fc}A_{clt,fc}$ | 28000 | W/K |
| $h_{c,clt,hex}A_{clt,hex}$ | 6445 | W/K |
| $\dot{m}_{clt}$ | 1.4 | kg/s |
| $\dot{m}_{air}$ | 1.25 | kg/s |
| $m_{air,hex}$ | 0.4334 | kg |
| $m_{clt,fc}$ | 15.6 | kg |
| $m_{fc}$ | 400 | kg |
| $m_{hex}$ | 20.4 | kg |

Table A.6: Thermal system parameters

| Parameter | Value | Units |
|---|---|---|
| $M_{Carbon}$ | 12.0107 | g/mol |
| $M_{Flourine}$ | 18.9984032 | g/mol |
| $M_{Hydrogen}$ | 1.00794 | g/mol |
| $M_{Nitrogen}$ | 28.0134 | g/mol |
| $M_{Oxygen}$ | 15.9994 | g/mol |
| $M_{Sulfur}$ | 32.065 | g/mol |

Table A.7: Nitrogen permeation parameters